International Journal of Fatigue 206 (2026) 109452

Contents lists available at ScienceDirect

International Journal of Fatigue

journal homepage: www.elsevier.com/locate/ijfatigue

Fatigue life prediction of multi jet fusion-manufactured polyamide12 lattice structures using the average strain energy density method

Raffaele De Biasi [a,b,*], Lorenzo Romanelli [c], Ciro Santus [c], Matteo Perini [d], Filippo Berto [a], Matteo Benedetti [b]

[a] Department of Chemical Engineering Materials Environment, Sapienza University of Rome, Via Eudossiana 18, 00184 Roma, Italy
[b] Department of Industrial Engineering, University of Trento, Via Sommarive 9, Trento 38123, Italy
[c] Department of Civil and Industrial Engineering, University of Pisa, Largo Lucio Lazzarino 1, Pisa 56122, Italy
[d] ProM Facility, Via Fortunato Zeni 8, Rovereto 38068, Italy

ARTICLE INFO

Keywords:
Multi jet fusion
MJF
Average stain energy density
PA12
Fatigue estimation
Lattice structures
Porosity analysis

ABSTRACT

The industrial sector continues to explore innovative strategies to exploit the full potential of Additive Manufacturing (AM). Among its many advantages, AM enables the fabrication of lattice structures; these are lightweight metamaterials with tunable mechanical properties and excellent energy absorption capabilities. Despite their promise, the widespread industrial use of such structures is limited by the difficulty in accurately assessing their fatigue behavior. This study presents a methodology aimed at predicting the fatigue life of polymer-based lattice components, with a specific focus on PA12 manufactured using the Multi Jet Fusion (MJF) process. This is an industrially relevant technology offering large production volumes, high printing quality and low production costs. The approach begins with fatigue testing of bulk PA12 specimens to establish baseline material behavior. Based on these results, a predictive algorithm is developed to estimate the fatigue performance of lattice structures. The model adopts an energy-based framework inspired by the Average Strain Energy Density (ASED) method, previously used for metallic materials, and adapts it to the characteristics of polymer lattices. The proposed methodology contributes to the development of efficient fatigue assessment tools, supporting the broader adoption of lattice structures in cost-sensitive industrial applications where polymer-based materials are effective.

1. Introduction

Additive manufacturing (AM), or 3D printing, is nowadays a well-established production methodology that spans from metals to polymers, offering a wide range of material properties that can be selected based on the specific application requirements. AM is commonly used for prototyping, particularly to reduce preparation times. Moreover, it represents the most suitable, or just the only, production technique for fabricating components with complex geometries. A clear example of this is the design and optimization of lattice structures [1–4], which find application in various fields due to their significantly reduced (relative) density. For this reason, latticization, i.e. the design approach of substituting a full dense material (or solid material) with a lattice, is an ideal solution for producing lightweight components, where highly stressed regions can still be manufactured as locally solid. Such an approach enables efficient topology optimization even at sub-millimetric scales. A notable application of this methodology is the fabrication of prostheses, such as for the forearm, that can be either solid or include lattice regions, depending on the required shape adaptation and performance optimization [5,6].

Polyamide 12 (PA12), also known as Nylon 12, is among the most widely used polymeric materials in AM, particularly for lightweight applications [7]. Compared to other polymers, PA12 offers several advantages, including excellent dimensional stability and surface quality, low porosity, high mechanical strength, and even biocompatibility. However, these properties are strongly influenced by the production method and the specific manufacturing parameters adopted [8–11]. PA12 can still be processed through conventional injection molding technique [12], but it is also compatible with modern AM technologies, such as Selective Laser Sintering (SLS) [13,14] and Multi Jet Fusion (MJF) [15,16]. The SLS and MJF processes are conceptually similar to Laser Powder Bed Fusion (L-PBF) used for metals, i.e. they belong to the

* Corresponding author.
E-mail address: raffaele.debiasi@uniroma1.it (R. De Biasi).

https://doi.org/10.1016/j.ijfatigue.2025.109452
Received 21 July 2025; Received in revised form 26 November 2025; Accepted 18 December 2025
Available online 21 December 2025

category of "powder-based" techniques, and for both SLS and MJF, it is possible to reuse part of the unprocessed powder [17–19]. In SLS, polymer particles are sintered rather than fully melted, and this approach is well-suited to thermoplastic materials, unlike metal-based L-PBF which involves complete fusion. On the other hand, MJF is a powder-based AM technique developed by HP that does not involve lasers. Instead, it uses inkjet-style printheads to selectively deposit a fusing agent, plus another detailing agent, onto a powder bed. An infrared lamp then passes over the surface, to fuse just the areas treated with the fusing agent, as schematically illustrated in Fig. 1.

Experimental comparisons of the mechanical strength of PA12 produced via SLS and MJF are widely reported in the recent literature. In some studies, both techniques are directly compared, while others focus on just one of the two, analyzing specific aspects such as viscoplastic behavior, the influence of printing orientation, and the thermal cycles involved in the process [20,22–28]. In terms of static strength, typically expressed as ultimate tensile strength (UTS), both techniques are characterized by similar values, generally in the range of 40–50 MPa. However, more significant differences can be observed in the elongation at fracture, especially depending on build orientation. For instance, Rosso et al. [26] found that, for specimens tested along the build direction, MJF parts exhibited up to twice the ductility compared to SLS, and this trend was also confirmed by Sillani et al. [23]. On the other hand, Cai et al. [20] reported similar elongation values for both techniques, around 15 %, along the same Z direction (i.e. the specimen axis aligned with the build direction). An opposite behavior was reported by Xu et al. [24], who found significantly higher elongation for SLS (approximately 30 %), nearly double that of MJF. In the case of SLS, the X and Y directions (referring to the ISO/ASTM 52,921 orientation scheme for specimens) yielded nearly identical results, while for MJF, the elongation was notably higher along X, followed by Y and then Z. However, O'Connor et al. [16] reported a reversed X vs. Y trend compared to Cai et al., highlighting inconsistencies possibly due to processing conditions or measurement methods. In summary, MJF PA12 typically exhibits UTS values of 40–50 MPa and elongation at fracture in the range of 15–25 %, although these properties can be strongly affected by several factors [29], including the part's position within the building chamber, which influences local crystallinity [30]. Young's modulus also appears to exhibit low repeatability. O'Connor et al. [16] reported values between 1100 and 1200 MPa, with the Z direction being only slightly stiffer. In contrast, Cai et al. [20] found higher values, around 1300 MPa for the X and Y directions, and over 1600 MPa along Z.

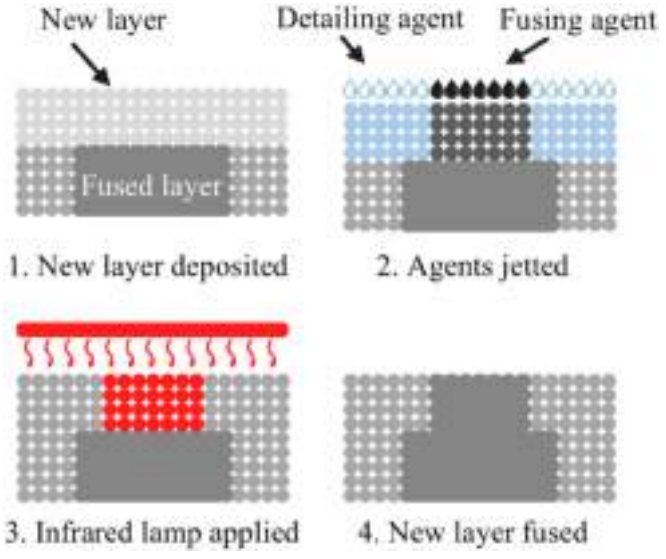

Fig. 1. MJF printing process phases for producing parts in PA12, after [15,16,20,21].

Similarly, high stiffness values were observed by Perez-Barcenilla [31], who also reported Poisson's ratio values in the range of approximately 0.35–0.38.

Fatigue strength is obviously another key factor in the design of lightweight components, particularly when polymeric materials are involved. Many fatigue models originally developed for metals can also be applied to polymers, including the Basquin model (for high-cycle fatigue, HCF), the Coffin-Manson model (for low-cycle fatigue, LCF) [32], the Paris' law for crack propagation [33,34], and those formulations accounting for mean stress effects [35]. However, polymers exhibit certain differences compared to metals, such as a marked sensitivity to loading frequency [36], which is an effect that is typically negligible in metal alloys. Moreover, the loading orientation with respect to the build direction is again a critical variable to consider in fatigue testing of PA12, for both SLS and MJF processes [37–39]. Another established tool in the fatigue analysis of conventionally manufactured metals is the Kitagawa-Takahashi diagram [40,41], which has more recently been extended to additively manufactured metal alloys [42,43]. In this approach, the threshold defect size is often expressed as the square root of the projected area of the critical flaw, which in AM materials is typically related to porosity. The Kitagawa-Takahashi framework has also been successfully applied to PA12, both in its injection-molded and SLS-processed forms [44].

Schob et al. [45] tested SLS-manufactured PA12 specimens using a test frequency of 3 Hz to minimize temperature increase during fatigue loading. The specimens were fabricated in a horizontal orientation, i.e. with their longitudinal axis perpendicular to the build direction. Under higher imposed stress amplitudes, a pronounced strain softening behavior was observed. The fatigue endurance limit was found to be below 20 MPa for a fatigue life of approximately $.2 \times 10^5$

cycles. Similarly, Van Hooreweder and Kruth [46] and Van Hooreweder et al. [47] tested SLS PA12 again at relatively low frequencies, 1 Hz and 3 Hz, reporting negligible differences between these two conditions. Strain softening was also observed, and a fatigue endurance limit of approximately 18 MPa at 10^6 cycles was found. Interestingly, this value remained nearly constant across the $10^5 - 10^6$ number of cycles to failure, indicating a sort of fatigue limit. Similar values were also observed by D'Andrea et al. [48] by testing MJF PA12 at load ratio 0.1 and 1 Hz and observing 30 MPa and 22.6 MPa for unaged and aged specimens, respectively. MJF-manufactured PA12 mechanical properties were extensively studied by Chen et al. [39], who tested both plain and lattice specimens. They also investigated the influence of build orientation, comparing vertical specimens (i.e. along the build direction) with horizontal ones. Consistent with previous studies, they reported UTS values in the range of 40–50 MPa. Elongation at fracture was significantly higher for horizontally built specimens (approximately 25–30 %), whereas vertically built specimens showed values slightly above 10 %. In terms of fatigue behavior, their results were comparable to those obtained for SLS PA12 in the previously mentioned studies, although the fatigue regime explored was limited to low-cycle fatigue (LCF) and a load ratio of $R = 0$ instead of $R = -1$. Nevertheless, a clear influence of build orientation was confirmed: horizontally built specimens exhibited superior fatigue performance, consistent with their higher ductility in monotonic tensile tests. This behavior was attributed to the orientation of voids (or pores) within the material. In vertically built specimens, the projected area of such defects perpendicular to the loading direction was larger, leading to lower fatigue strength. However, the sensitivity to building orientation was almost entirely mitigated in lattice structures. In this situation, the inherent geometric irregularities at the strut junctions (which act as stress concentration sites) dominated the fatigue response, effectively masking the influence of build direction. And this situation is very similar to that investigated in the present paper, where the notch effect is a key factor to be considered and experimentally quantified.

Notch sensitivity in polymers can be analyzed using the same

methodologies commonly adopted for metals, such as the Theory of Critical Distances (TCD) and the Averaged Strain Energy Density (SED or ASED) approach. For example, the TCD has been successfully applied to additively manufactured polylactide (PLA) in both monotonic and fatigue strength assessments [49,50]. It has also been used for SLS PA12 in fracture tests by Crespo et al. [51], and for MJF PA12 by Avanzini et al. [52]. In both cases, and for specimens fabricated in the parallel (horizontal) orientation, a similar critical distance L was found, in the range of approx. 0.6–0.8 mm. It is worth noting that they obtained the TCD by combining the strength of notched specimens with different levels of severity, i.e. different notch radii. This methodology is well established for evaluating monotonic (static) strength [53], although the outcome may be sensitive to the choice of the "sharp" and "blunt" specimens used to determine the material parameter, as noted by comparing the results by Crespo et al. and Avanzini et al. Under fatigue loading, however, it is more common to combine the results of plain specimens with those of sharply notched ones [53]. A dedicated procedure based on this principle was proposed by Santus et al. [54,55] and later extended to out-of-plane (mode III) loading conditions [56]. Nevertheless, the use of two notched specimens can still be effective in cases where plain specimen fatigue data are unavailable or unreliable, such as in thick-walled ductile cast irons, where large shrinkage pores may dominate over more uniformly distributed defects like graphite nodules [57]. This approach can, in principle, also be extended to additively manufactured materials, whether metallic or polymeric, in case of such defectiveness.

As an alternative to TCD, the ASED approach can be adopted particularly for components with complex geometries, since the averaging is conducted over a finite area or volumetric region, rather than a single point or along a line [58], unless the Area or the Volume methods are considered instead of the Point or the Line methods. And, indeed, in the present paper, the lattice structure introduces a complicated geometry which shows three-dimensional details that are comparable in size with the so-called control radius. For this reason, the ASED was considered more promising to predict the fatigue strength of PA12 lattice components. Again, a methodology for determining the control radius was proposed by Benedetti et al. [59] and applied to both conventionally and additively manufactured metals [60], also accounting for the influence of the standard deviation in experimental results used for the inverse estimation of the control radius. This approach was extended to mode III loading conditions as well [61]. An inversion procedure based on two notches, one sharp and one blunt, was also implemented for the ASED methodology [62]. In principle, multiaxial stress states should be modelled using different control radii for each mode and then combined [63]. However, a simplified approach can be adopted based solely on the mode I parameters, even in the presence of a secondary mode III component [64]. The ASED predictive technique has been applied to the fracture behavior of MJF-manufactured PA12 by Avanzini et al. [65]. Additionally, Zolfagharian et al. [66] applied it to nylon samples fabricated using fused deposition modelling (FDM), alongside MJF specimens, demonstrating its applicability to various polymeric additive manufacturing processes. These latter papers show the ASED potentiality on this material just on solid samples. However, this methodology was never extended to a fully three-dimensional geometry manufactured in PA12. On the contrary, in the present work, the fatigue behavior of MJF-manufactured PA12 specimens is initially investigated with solid samples, and then the ASED prediction is performed at the nodal points of a complex lattice structure where the stress concentration shows a three-dimensional characteristic.

This paper is structured as follows. Section 2 initially presents the lattice structure under consideration. V-notched specimens are also introduced, following the geometrical configurations proposed in [54,55,59]. Section 3 shows the quasi-static test on plain specimen. Computed tomography (CT) scans are performed on the fatigue specimens, to better understand the effects of the manufacturing defects. The ASED control radius, along with the critical strain energy density range, are determined under mode I fatigue loading. The lattice structure previously introduced is then modelled with finite element method (FEM) and the sub-modelling technique. The stress concentrations occurring at the lattice nodes are analyzed using the ASED methodology with the previously calibrated parameters. Finally, in the Conclusions section the obtained results and the accuracy of the prediction are summarized and discussed.

2. Materials and methods

In the following section, a definition of the lattice geometry and the associated bulk specimens for fatigue life characterization is provided alongside the description of the testing equipment and the metrological set-up. Moreover, a definition of the algorithm for fatigue prediction is discussed and details on the finite element simulations associated are given.

2.1. Specimen design and fabrication

To realize the lattice components, an industrial relevant solution was employed. The Multi Jet Fusion (MJF) technology developed by HP was selected for the possibility of manufacturing components without the need for support structures, namely a HP MultiJet Fusion 4200 equipment was used. The commercially available PA12 material (HP 3D High Reusability PA 12) was selected for its industrial relevance and for economic sustainability. The reasoning behind the design of the lattice specimens used in this study is illustrated in Fig. 2. The design was initially inspired by ASTM D638 to guarantee consistency and reliability in evaluating mechanical performance. The base structure consisted of a cyclic X-shaped strut lattice, as shown in Fig. 2(a). The gauge section, typical of a standard bulk specimens, was designed with constant strut diameter and helix angle to ensure uniform tensile properties, thus enabling controlled and repeatable responses under tensile load. In the transitional zones, a gradual increase of the cross-section enhanced tensile strength and effectively distributed stress, reducing the risk of failure under high strain conditions. The transitional zones enabled smooth geometric transitions, of both helix angle and strut diameter, to avoid sudden compliance changes, supporting dependable mechanical assessments and robust structural behavior during tensile loading. In particular, the transition of the helix angle was governed by a linear function while the variation of the strut diameter was described by a quadratic polynomial. This latter choice enabled us to obtain a null gradient of the function at the interface between transitional and central zones thus providing the continuity of the first derivative and avoiding possible abrupt failures. The smooth variation of the relative angles of the X-shaped struts enabled the regulation of the transverse deformation, thus improving structural response by promoting bending and reducing transverse stiffness. Based on these design concepts, a lattice specimen was designed and manufactured, and it is reported in Fig. 2(b). In the specimen of Fig. 2(b), the cyclic base lattice incorporated a setup of X-I struts. The I struts bore the tensile loads, while the X struts constrained transverse deformation achieving a discretized beam-to-shell effect. Another important topic regarding the tensile tests of such lattice specimens is the design of the clamping system. The most relevant geometric quantities for the manufacturing of the lattice specimens are reported in Figs. 2(a) and (b), and their corresponding numerical values are shown in Table 1. Fig. 2(c) illustrates the tailored grips, to transfer tensile loads during the tests, in their mounted configuration. The design was inspired by ASTM D638 standard with a metal insert and an external clamp fastened with three M5 screws to ensure a firm, slip-free hold and stability throughout all the phases of the tests. Finally, to achieve a secure setup, the bolts were tightened while simultaneously pulling the fixture bars in opposite directions to ensure proper clamping and reduce backlashes.

The fatigue testing campaign on lattice specimens was completed by the characterization of the fatigue behavior of the base material. For this purpose, axisymmetric specimens, whose geometry is shown in Fig. 3,

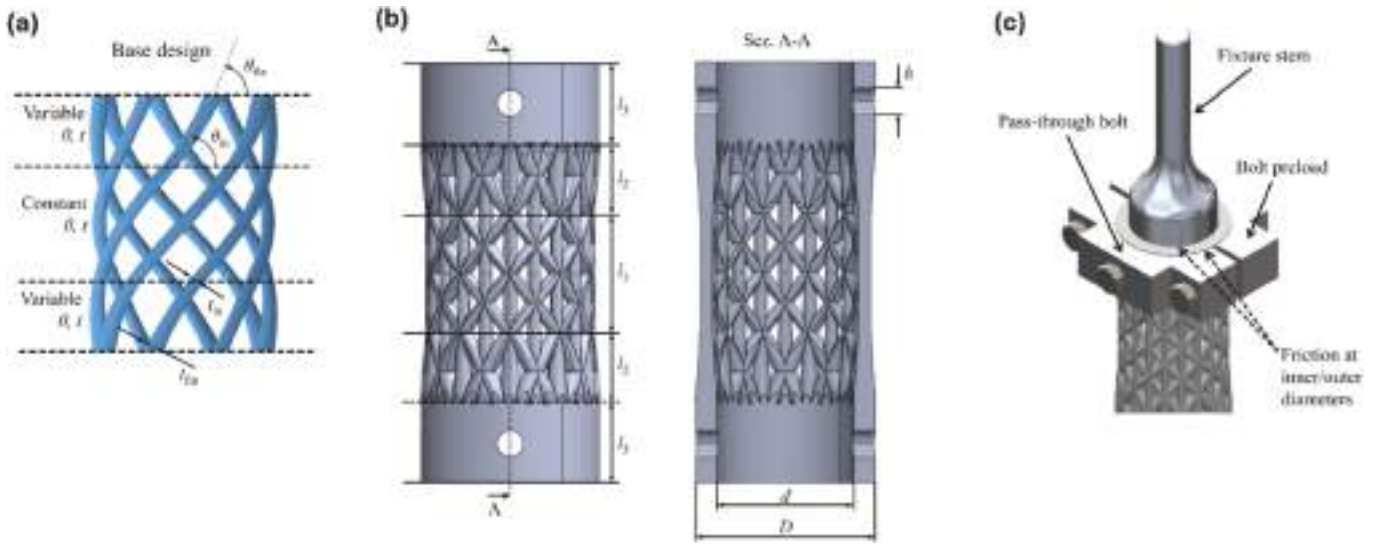

Fig. 2. a) design of the lattice specimen gauge and transitional zones. b) lattice specimen geometry for fatigue testing. c) gripping system for connecting the lattice component to the testing machine.

Table 1
Nominal dimensions of the geometric quantities of the lattice specimens reported in Fig. 2(a) and (b).

t_{in} – mm	t_{fin} – mm	θ_{in} – deg	θ_{fin} – deg	l_1 – mm
2.4	3.2	50°	70°	22.6
l_2 – mm	**l_3 – mm**	**D – mm**	**d – mm**	**h – mm**
13.7	15	34	26	5

were 3D-printed via MJF. In particular, plain specimens were fabricated and tested to evaluate the impact of big, isolated porosity on fatigue behavior. Besides, two notched specimen geometries, with different severity (one called "blunt" and the other "sharp") were manufactured and tested to evaluate the fatigue properties of a nearly defect free material, as discussed in Section 3.3.

2.2. Quasi-static mechanical characterization

To characterize the quasi-static mechanical response of the bulk specimens, one plain specimen was tested with a hydraulic uniaxial machine, namely an Instron 8516 equipped with a 100 kN load cell. The test was position controlled, and a speed of 0.6 mm/min was set. During the test, an extensometer with gauge length equal to 10 mm was applied in the central part of the specimen to improve the deformation measurement.

2.3. Defect characterization

To characterize the components' defectivity two techniques were developed: the fracture surfaces of the specimens were analyzed with a Scanning Electron Microscope (SEM) JEOL JSM-IT300LV, while one specimen for each geometry underwent CT scan. This technique is able to provide a three-dimensional reconstruction of the geometry, including internal porosity and surface defects. The equipment used was a Zeiss Metrotom and the scan characteristics are listed in Table 2. To analyze the three-dimensional geometrical reconstruction the 3D image analysis software ORS-Dragonfly (Comet Technologies Canada Inc, Canada) was used.

Table 2
CT scanning parameters adopted in the analyses of bulk and lattice specimens.

Voltage – kV	Current $-\mu A$	Voxel size $-\mu m$	Cu physical filter – mm	Nr. Projections
200	242	39.09	0.5	2050

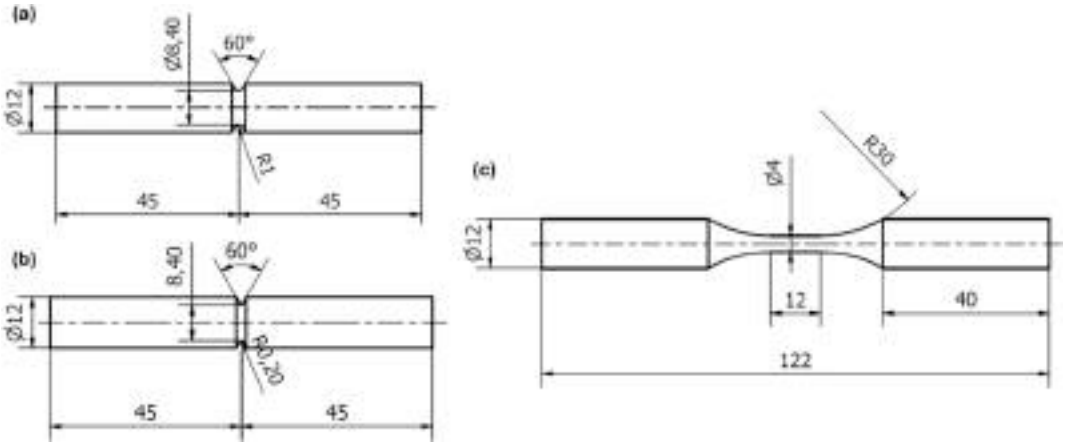

Fig. 3. Geometries designed for the fatigue investigation of the lattice base material (MJF – HP 3D High Reusability PA 12), namely specimen characterized by sharp notch (a), blunt notch (b), and plain specimen (c). Dimensions in the drawings are reported in mm.

2.4. Fatigue testing

Fatigue tests on lattice and bulk specimens were carried out with an electrodynamic testing machine StepLab UDO20 equipped with a 20kN load cell and mechanical grips. Each specimen was subject to a load-controlled sinusoidal fully reversed (R = -1) stress cycle at 5 Hz. Fatigue tests terminated either with complete separation of two broken parts or in run-out tests after 1 million load cycles. Runout specimens were tested again at a stress at least 1.5 times higher than the runout stress to obtain additional data points. The S-N curves of the lattice material were constructed using 15 specimens, while at least 12 fully dense specimens with either plain or notched geometry were tested to characterize the base material.

The data were fitted either with a Basquin curve (Equation (1a) or with a power law with asymptotic term (Equation. (1b) depending on the presence or not of a knee before 10^6 cycles.

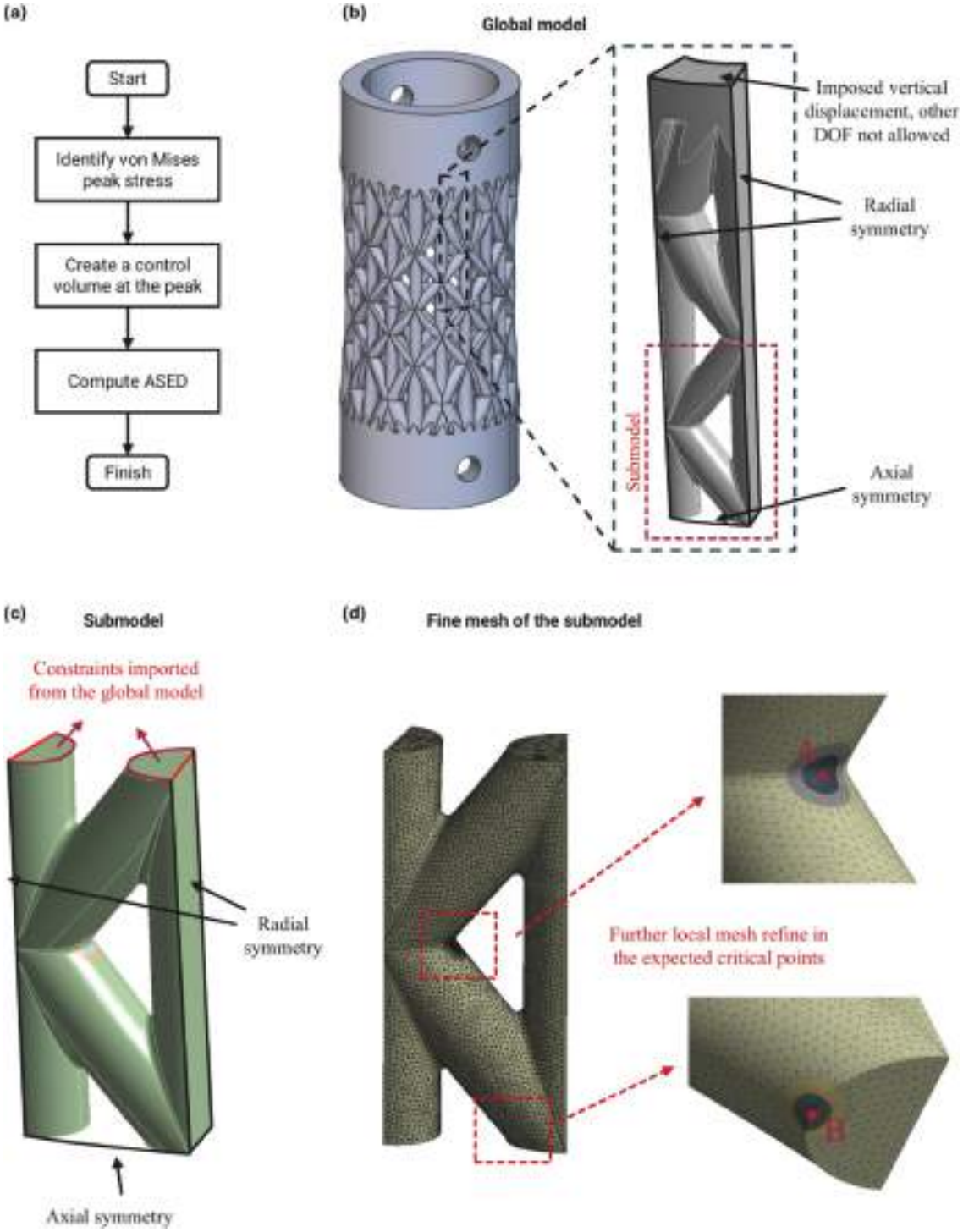

Fig. 4. a) workflow proposed for average strain energy density based critical location identification and fatigue life estimation. b) symmetrical finite elements model developed for the identification of the critical location of the specimen geometry. given the limited impact of manufacturing induced defects in the selected manufacturing technology, the simulation is based on the as-design lattice geometry.

$$\sigma_a = \frac{c_1}{N_f^{c_2}} \tag{1a}$$

$$\sigma_a = \frac{c_1}{N_f^{c_2}} + c_3 \tag{1b}$$

Lattice specimens' data, collected as force vs. number of cycles to failure were normalized in terms of homogenized stress vs. number of cycles to failure by dividing the measured forces by the area of the middle section of lattice specimens, in agreement with [6].

The scatter of the fatigue data was assessed by computing the estimated regression variance assumed to be uniform for the whole fatigue life range and expressed by:

$$S^2 = \frac{\sum_{i=1}^{n} \left(\sigma_{a,i} - \widehat{\sigma}_{a,i}\right)^2}{n - p} \tag{2}$$

where $\sigma_{a,i}$ is the i-th fatigue amplitude data point, $\widehat{\sigma}_{a,i}$ is its estimator, n is the number of data elements, and p is the number of parameters in the regression; p = 2 and 3 for Equation (1a) and (1b), respectively. To distinguish the struts failed by fatigue from those failed by static tension, the fracture surfaces are investigated under SEM.

2.5. Fatigue life estimation

It is already proved the possibility to apply the Average Strain Energy Density Method to the fatigue prediction of lattice structures [58]. However, the method was developed for Laser-Power Bed Fusion (L-PBF) components where fatigue failure is driven by the presence of manufactured induced defects. In contrast, the MJF manufacturing technique is less prone to generate critical surface defects, namely partially melted particles and parasitic masses that deeply impact the geometry of the component. For this reason, a novel and leaner algorithm for the identification of the critical locations is proposed. This procedure leverages the fact that MJF defects are not the driving mechanism able to promote fatigue failure, in contrast in these components the critical locations are identified by the geometrical characteristics of the component itself. In this ideal condition, fatigue failure depends on the as-design geometry of the component rather than on the defect distribution. For this reason, the proposed approach is closer to what can be an ideal approach to the fatigue life estimation in lattice structures.

In the methodology, contact points can be found with the procedures identified in [58], however, the limited impact of the material defects allows us to base fatigue predictions on the as-design geometry and therefore do not require the usage of the as-built geometry reconstructed with micro-CT technology. The proposed procedure is presented in Fig. 4a: thanks to a finite element simulation the most critical location in the analyzed geometry is identified by computing the maximum of the von Mises stresses. This is then identified as critical location, and the location of the stress peak is used to center the control radius required by the ASED method. In accordance with Equation (3), the ASED is computed in the identified region, and this value can be compared with the reference curve associated with the material to access component fatigue resistance.

$$ASED = \frac{\sum_{\Omega} W_e * V_e}{\sum_{\Omega} V_e} \tag{3}$$

In this expression, W_e refers to the strain energy density of the e-th finite element within the critical domain Ω, while V_e denotes the corresponding elemental volume.

The implemented FE model to calculate the ASED values is presented in Fig. 4. Firstly, a global model, representing 1/40 of the lattice specimens thanks to symmetries, was implemented as described in Fig. 4b. The constraints used in the global model consisted of radial symmetries on the lateral faces and of an axial symmetry on the lower face. Finally, on the upper face a vertical displacement was imposed and the other degrees of freedom, i.e. displacements and rotations, were imposed as null. These latter constraints on the upper face were coherent with the boundary conditions imposed during the experimental tensile tests. Once the global model was solved, a submodel was implemented, as shown in Fig. 4c, considering the portion of the global model contoured in red in Fig. 4b. The constraints imported from the solution of the global model were applied to the upper surface of the submodel, while the symmetries, both radial and axial, were applied to the other surfaces coherently with the global model. To enhance the accuracy of the solution, the mesh of the submodel was refined with respect to the corresponding mesh of the global model. In addition, a further spherical refinement of the mesh, with centers in points A and B, was implemented as shown in Fig. 4d. More details on the mesh convergence analysis can be found in Appendix A1 of the paper. Points A and B of Fig. 4d corresponded to the potential critical zones of the structure. Finally, once the solution of the submodel was obtained, the Von Mises stress peak point was detected. The linear elastic FE models were developed in ANSYS mechanical (ANSYS 2024 R1, USA) and relies on quadratic tetrahedral solid elements (SOLID 187).

3. Results and discussion

3.1. Quasi static mechanical properties

To verify the consistency of the material properties, a bulk specimen is tested under quasi-static loading conditions using the experimental setup detailed in Section 2.2. Among the geometries considered in this study, a plain specimen — whose shape closely resembles the standard dog-bone profile — is selected for this analysis. The experimental set-up is depicted in Fig. 5a, where the position of the extensometer can be observed. The results of the test are reported in Fig. 5b, showing a mechanical response consistent with the expected behavior of PA12. The stress–strain curve exhibits an initial linear region, followed by a deviation from linearity as plastic deformation occurs. This behavior is in good agreement with literature results on the same material and on similar specimen geometry. The Ultimate Tensile Stress (UTS) is in agreement with [6,26,65,67,68] and the elongation is also consistent. For this reason, the mechanical properties considered in the finite element simulations are listed in Table 3 and are consistent with [6].

3.2. Defectiveness

Right after the manufacturing process, to access the printing quality of the components, one specimen for each geometry is randomly picked and underwent CT scan analysis as reported in Section 2.3. A complete three-dimensional reconstruction of the component geometry is obtained, and specific focus is given to the defects identified in the gauge region of the bulk specimens, as well as in the central part of the lattice one. It is well known how manufacturing induced defects are critical to fatigue resistance in additive manufacturing components; therefore, the analysis is limited to the highly stressed regions where fatigue failure occurs. The analysis focuses on internal porosity, as this manufacturing technique often produces components with a dispersed distribution of pores within their internal regions. These defects typically appear in two forms: spherical cavities, known as keyholes, and elongated ones, referred to as lack-of-fusion pores. The latter may also contain partially melted particles, resulting from an uneven distribution of fusing and detailing agents during the printing process [67,69]. Figs. 6 and 7 depict the three-dimensional reconstruction of the bulk specimens' geometries and the associated porosities analysis for blunt and sharp specimens respectively. Fig. 8 is devoted to the three-dimensional geometry reconstruction of the plain specimen, while Fig. 9 is focused on the analysis of the lattice specimen. In all of the four analysis, pores are characterized by three different parameters: Feret diameter, corresponding to the diameter of the maximum sphere that can include the

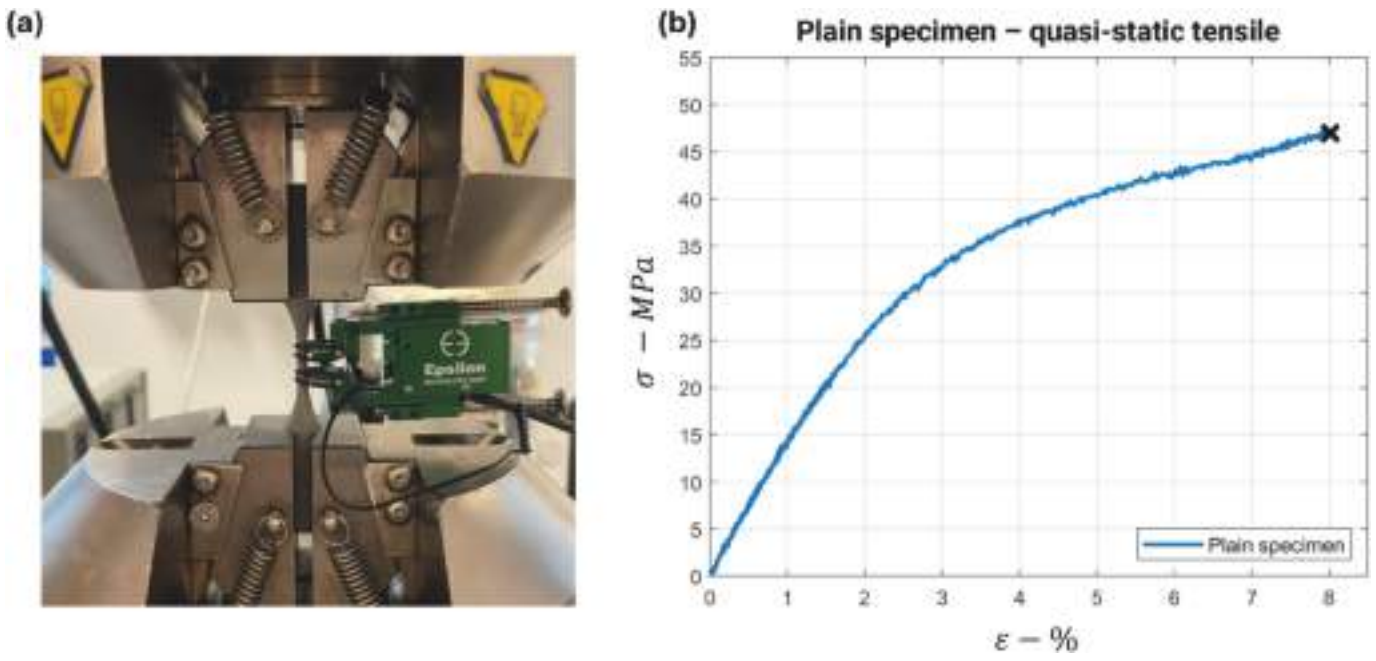

Fig. 5. Experimental set-up (a) and stress–strain curve (b) of the quasi-static test on plain specimen.

Table 3
Material properties identified for PA12 material finite elements simulation.

Material	E – MPa	υ– #
PA12	1119.9	0.45

defect; Sphericity, which is computed as the ratio between the defect volume and the defect surface area; and $\sqrt{area}$, computed in agreement with Murakami's theory [70], projected on the plain orthogonal to the loading axis.

A statistical analysis is performed on these quantities, to easily compare the pore population of the three different specimens. Results are displayed in Figs. 6, 7, 8, and 9 and collected in Table 4. A Gaussian distribution is fitted in the measured data, and to improve data representation, the median is also included in the analysis.

There is a clear consistency between the three bulk specimens, both in pore size (Feret diameter and $\sqrt{area}$) and pore shape (sphericity). All samples exhibit a distribution of small, nearly spherical pores concentrated mainly in the central region, as shown in Figs. 6a, 7a and 8a. This pattern is unlikely to be accidental and is instead related to the manufacturing process. The action of the detailing agent along the component edges creates an external layer with virtually no porosity, while the inner core contains a dense and uniform distribution of pores. This effect is typically associated with suboptimal printing parameters and leads to an unusual defect distribution. The observation of characteristic dispersed porosity is also found in literature data: Calignano et al. [67] analyzed MJF-printed PA12 tensile specimens via CT-based reconstruction and reported a pore population with high sphericity and an average Feret diameter of 0.19 ± 0.03 mm. This is called "intralayer porosity" [69] and can be appreciated in the fracture surfaces of specimens failed under fatigue solicitations [26].

The three-dimensional reconstruction of the lattice specimens reveals both similarities and distinctive features. First, an intralayer porosity with dimensions comparable to those found in the blunt and sharp specimens is detected. These pores constitute the main porosity population, as confirmed by the median Feret diameter, which matches the values measured in the bulk samples. However, this finer porosity is accompanied by larger defects with lower sphericity, which can be attributed to lack-of-fusion phenomena. These larger pores are particularly detrimental to fatigue performance. Nevertheless, as shown in Fig. 9a, porosity is again concentrated in the core of the lattice struts, while the outer shell exhibits higher printing quality and remains largely free of defects.

After this preliminary analysis, the specimens are subjected to fatigue tests, and the fracture surfaces are investigated under SEM technology; results are depicted in Fig. 10. For this analysis, the set-up listed in Section 2.3 is employed and a specimen for every different batch is selected so that the failure is encountered at $N_f \in [10^5; 10^6]$. Selected specimens are represented with a star in Fig. 10.

Figs. 10a and 10b refers to the fracture surfaces of the sharp and blunt notched specimens respectively. Blunt specimen in Fig. 10b reached run-out condition while about to fail and was subjected to cryogenic rupture to expose the fracture surface. Both these specimens are characterized by fatigue failure nucleating near the surface [71], in correspondence of the specimens at the notch tip, where the loading conditions are most critical. In agreement with the observations of [26], the fracture surface is characterized by the presence of two distinct regions: a smoother and planar region where the crack advances and a rougher area, often characterized by plane changes and porosity characteristic of the final failure of the component. These areas are clearly depicted in Fig. 10a, where the crack nucleation stared on a surface defect in the sharp notched specimen on the left and propagated in a circular shape in the crack propagation stage, till reaching the material resistance limit and the complete failure generating the rougher surface on the right side of the Figure. In contrast, the failure of the blunt specimen analyzed in Fig. 10b, is traced back to the presence of a near surface lack of fusion pore, as depicted in the magnification detail. The crack propagation proceeds in the lowermost part of Fig. 10b while the upper, sharp and planar side of the specimen is characteristic of the cryogenic rupture imposed on this specimen. Fig. 10c depicts the fracture surface of the plain specimen; the specimen presents a double initiation crack sites, starting from two different planes and coalescing into a diagonal fracture surface following the position of a pre-existing porosity. Intralayer porosity can also be detected in this specimen. The initiation location is identified in a sub-surface pore cluster as highlighted in the magnification image. The crack growth follows the presence internal porosity deviating the crack path on multiple plans. The fracture surface of a lattice structure strut is presented in Fig. 10d. The

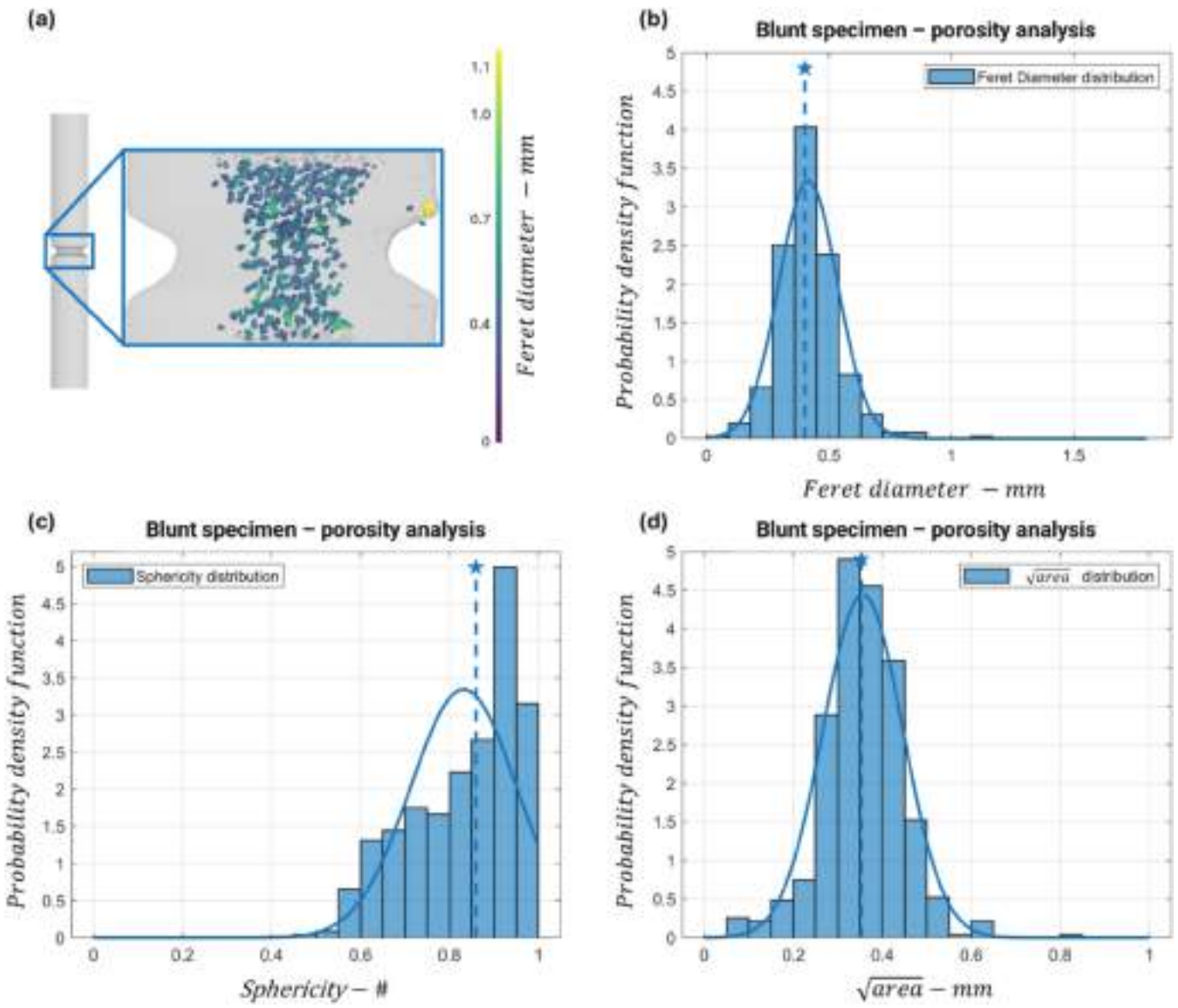

Fig. 6. Three-dimensional CT-based geometrical reconstruction of the blunt notched specimen (a) and the results of the associated porosity analysis: Feret diameter (b), Sphericity (c), and $\sqrt{area}$ projected on the plain orthogonal to the loading direction (d). Defect distribution is characterized by a statistical analysis, showing the Gaussian distribution and the median (with a star) associated with the measured data.

fracture surface is characterized by a planar and smooth appearance, typical of the crack initiation and propagation in polymeric materials. This failure is initiated by a defect on the contour of the geometry, and the absence of a rougher surface texture denotes the absence of the final fracture in this specific strut. Also in this component, as described for the others, the presence dispersed intralayer porosity is detected: small pores equally present on all fracture surfaces.

3.3. Fatigue properties: Intrinsic fatigue strength, control volume radius and El Haddad-Smith-Topper parameter

The different specimens' geometries are tested under fully reversed fatigue conditions, as per specifications provided in Section 2.4 and results are charted in terms of stress amplitude vs. number of cycles to failure in Fig. 11. Notably, the fatigue resistance of geometry characterized by a sharp notch (Fig. 11b) is reduced if compared to the blunt notch geometry (Fig. 11a). Moreover, there is a little variation in the fatigue resistance of notched and plain specimens (Fig. 11c), indicating a strong influence given by the manufacturing induced defects in the plain specimens. Lattice fatigue data in Fig. 11d are presented in terms of stress amplitude accordance with the quasi-static results presented in Section 3.1. Fatigue data are fitted as per Equation 1 and scatter bands representing the 90 %-10 % failure probability are provided. Fitting parameters are listed in Table 5.

A direct comparison with the literature is not straightforward, as the available fatigue data for MJF PA12 were obtained at different load ratios. While our tests were performed under fully reversed loading (R = –1), the works of Rosso et al. and Avanzini et al. [26,52] report results for R = 0 and R = 0.1. These conditions are generally more damaging because the larger tensile portion of the cycle enhances crack opening and typically reduces fatigue strength. Nevertheless, the literature data still outperform our plain-specimen results. This discrepancy highlights the significant influence of manufacturing-induced defects in our samples, which markedly reduce their plain fatigue strength.

Based on this preliminary analysis, the focus is shifted to identifying the reference curve and the control radius R_1 for applying the ASED method to PA12. Since the plain specimens exhibit unfavorable manufacturing quality, the fatigue data from the two notched configu-

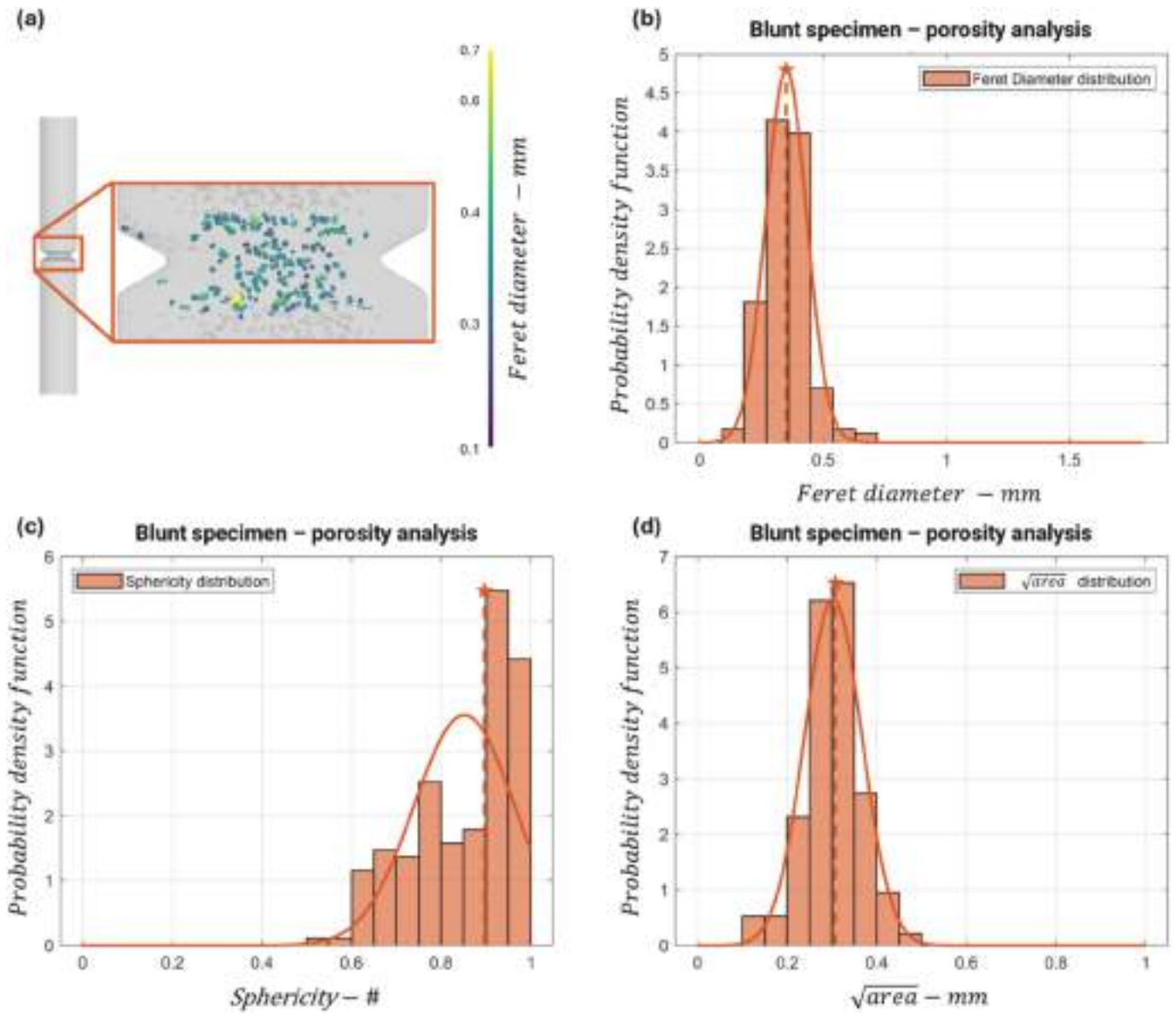

Fig. 7. Three-dimensional CT-based geometrical reconstruction of the sharp notched specimen (a) and the results of the associated porosity analysis: Feret diameter (b), Sphericity (c), and $\sqrt{area}$ projected on the plain orthogonal to the loading direction (d). Defect distribution is characterized by a statistical analysis, showing the Gaussian distribution and the median (with a star) associated with the measured data.

rations are used instead to characterize the fatigue behavior of a nearly defect-free material—i.e., material affected only by small, uniformly distributed intralayer pores, as discussed in Section 3.2. This strategy mirrors the approach adopted in [62] for nodular cast iron, a material with an analogous microstructural condition: a homogeneous distribution of graphite nodules in a metallic matrix, accompanied by a limited number of large shrinkage pores.

To extract the intrinsic fatigue properties, the two notched geometries are exploited because the stress field near their notch tips samples a small material volume with a high probability of being free from large defects. The method relies on the concept of average strain energy density within a control volume W, whose size is governed by the control radius R_1 (see sketch in Fig. 12). The intrinsic fatigue strength σ^*_{fl} of the material is used to define the notch fatigue concentration factor $K_{f,N}$, which is then inserted into the inverse function proposed in [60] to determine R_1.

$$R_1 = \frac{D}{2} f_{inversion}\left(\frac{R}{D/2}, \frac{\sigma^*_{fl}}{\sigma_{N,fl}}\right); K_{f,N} = \frac{\sigma^*_{fl}}{\sigma_{N,fl}} \tag{4}$$

The coefficients of the inverse function $f_{inversion}$ were recalibrated in this work to account for the Poisson ratio of PA12 ($\nu = 0.45$), which is not included in the original database of [60]. Additional details on the use of this inverse function are provided in Appendix A2.

CT scans pointed out that the large pores triggering failure in the plain specimens are not present at the notch root of the notched configurations, thereby leading to different fatigue damage mechanisms. Consequently, the fatigue strength σ_{fl} obtained from the plain geometry cannot be adopted as the intrinsic fatigue strength σ^*_{fl}. To address this issue, an inverse identification procedure based on the two notched configurations is applied, following the same rationale as in [62] Assuming that the sharp and blunt notches share the same control radius R_1, the following compatibility condition holds:

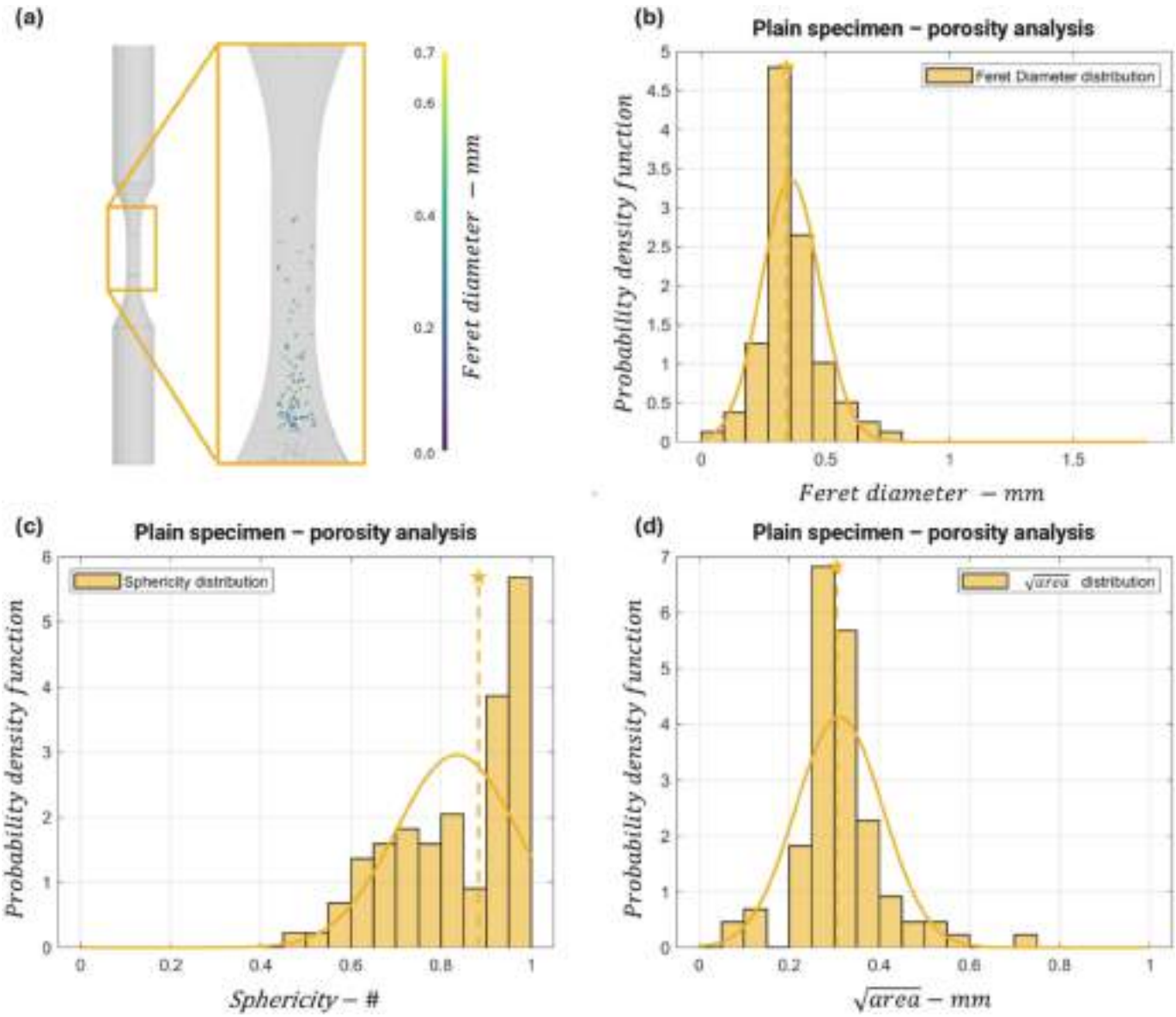

Fig. 8. Three-dimensional CT-based geometrical reconstruction of the plain specimen (a) and the results of the associated porosity analysis: Feret diameter (b), Sphericity (c), and $\sqrt{area}$ projected on the plain orthogonal to the loading direction (d). Defect distribution is characterized by a statistical analysis, showing the Gaussian distribution and the median (with a star) associated with the measured data.

$$\frac{D_{sharp}}{2} f_{inversion}\left(\frac{R_{sharp}}{\frac{D_{sharp}}{2}}, \frac{\sigma_{fl}^{*}}{\sigma_{sharp,fl}}\right) = \frac{D_{blunt}}{2} f_{inversion}\left(\frac{R_{blunt}}{\frac{D_{blunt}}{2}}, \frac{\sigma_{fl}^{*}}{\sigma_{blunt,fl}}\right) \tag{5}$$

Equation (5) contains a single unknown, σ_{fl}^{*}, which can be determined via an iterative root-finding procedure. Once σ_{fl}^{*} is identified, the control radius R_1 is directly obtained from Equation (4):

$$R_1 = \frac{D_{sharp}}{2} f_{inversion}\left(\frac{R_{sharp}}{D_{sharp}/2}, \frac{\sigma_{fl}^{*}}{\sigma_{sharp,fl}}\right) \tag{6}$$

The results of the double-notch inversion procedure are presented in Fig. 13a–b, where the control radius R_1 and the intrinsic fatigue strength σ_{fl}^{*} are plotted as functions of the number of cycles to failure. The mean values of these parameters were obtained using the mean fatigue properties of the two notched variants (50 % failure probability). Notably, the intrinsic fatigue strength is substantially higher than the fatigue strength measured on smooth specimens. This difference reflects the pronounced weakening effect of the large pores present in the plain specimens, which are absent at the notch root of the notched configurations.

The scatter band shown in Fig. 13b for the intrinsic fatigue strength was quantified through Monte Carlo simulations following the procedure outlined in [58]. This approach evaluates how the stochastic variability of the input fatigue properties (i.e., the fatigue strengths of the two notched variants) propagates to the output quantities, namely the intrinsic fatigue strength σ_{fl}^{*} and the control radius R_1. The input properties were modeled as Gaussian-distributed variables, from which random samples were drawn. For each sample pair, Eqs. (5) and (6) were solved to compute an individual realization of σ_{fl}^{*} and R_1. The resulting distributions were then ordered into quantiles, enabling the identification of the intrinsic fatigue strength at 10 % and 90 % failure probabilities.

To quantify the influence of manufacturing defects on the high-cycle fatigue strength of the plain specimens, a fracture mechanics approach based on the Kitagawa–Takahashi (KT) diagram [72] was adopted. In this framework, defects are modelled as cracks of effective size

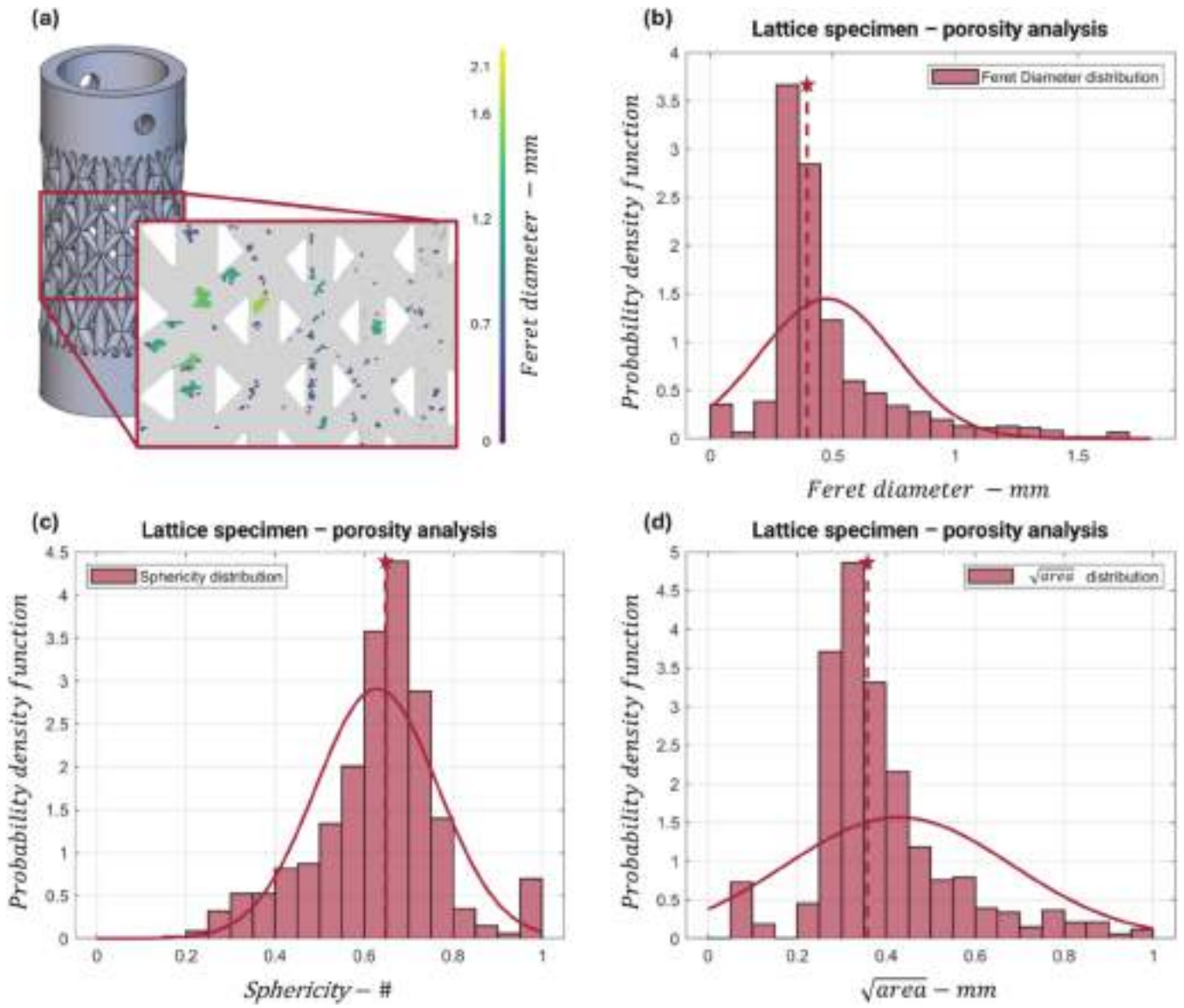

Fig. 9. Three-dimensional CT-based geometrical reconstruction of the lattice specimen (a) and the results of the associated porosity analysis: Feret diameter (b), Sphericity (c), and $\sqrt{area}$ projected on the plain orthogonal to the loading direction (d). Defect distribution is characterized by a statistical analysis, showing the Gaussian distribution and the median (with a star) associated with the measured data.

Table 4
Statistical analysis of the porosity identified in the CT-based geometry reconstruction.

	Geometry	Mean	Standard Deviation	Median
FeretDiameter $-mm$	Blunt notch	0.41	0.11	0.4
	Sharp notch	0.35	0.08	0.35
	Plain	0.36	0.12	0.34
	Lattice	0.47	0.27	0.39
Sphericity $-\#$	Blunt notch	0.83	0.11	0.85
	Sharp notch	0.85	0.11	0.89
	Plain	0.83	0.13	0.88
	Lattice	0.62	0.13	0.64
$\sqrt{\boldsymbol{area}}$ $-mm$	Blunt notch	0.35	0.08	0.35
	Sharp notch	0.30	0.06	0.30
	Plain	0.31	0.09	0.30
	Lattice	0.42	0.25	0.35

$$a_{eff} = Y^2 \bullet \sqrt{area} \tag{7}$$

where Y is the defect shape factor (0.5 for internal defects and 0.65 for surface-breaking defects), and $\sqrt{area}$ is Murakami's defect parameter [70], representing the square root of the projected defect area on a plane perpendicular to the loading axis.

The long-crack threshold stress-intensity-factor range ΔK_{th} was evaluated following the approach proposed by Lazzarin and Berto [73]. Under plane-stress conditions, ΔK_{th} is derived from the intrinsic plain-fatigue-limit range $\Delta\sigma_{fl}^{*} = 2\sigma_{fl}^{*}$ and the control radius R_1:

$$\Delta K_{th} = \Delta\sigma_{fl}^{*} \bullet \sqrt{\frac{4\pi}{5-3\nu}R_1} \tag{8}$$

Using this value, the El Haddad–Smith–Topper intrinsic crack length parameter [41] can be determined as:

$$a_0 = \frac{1}{\pi}\left(\frac{\Delta K_{th}}{\Delta\sigma_{fl}^{*}}\right)^2 \tag{9}$$

For a defect treated as a crack of effective size a_{eff}, the threshold stress range for non-propagation is then given by [74]:

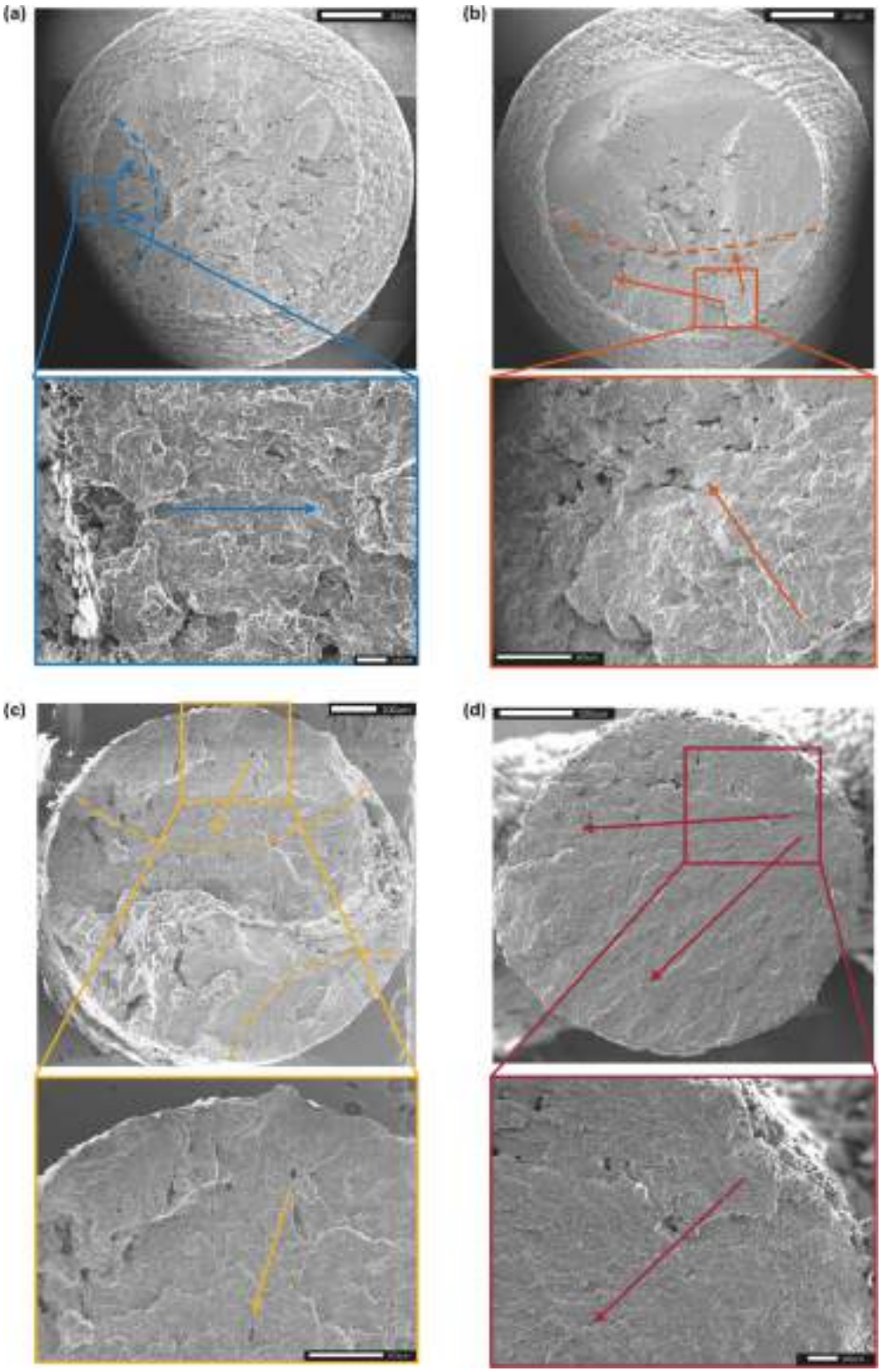

Fig. 10. Fracture surface analysis performed on SEM images for sharp (a), blunt (b), plain (c) and lattice (d) specimens. The arrows describe the crack propagation, and the dotted lines separate the crack growth region from the region characterized by the final failure.

$$\Delta\sigma_{th} = \frac{\Delta K_{th}}{\sqrt{\pi\left(a_{eff} + a_0\right)}} \tag{10}$$

Equation (10) is represented in the KT diagram shown in Fig. 14c, where $\Delta K_{\mathrm{th}} = 1.13\,\mathrm{MPa}\sqrt{\mathrm{m}}$ and $a_0 = 0.174\,\mathrm{mm}$. The corresponding scatter band was computed by propagating the 10–90 % dispersion of σ^*_{fl}.

Fig. 14c also reports the experimental high-cycle fatigue strengths of the plain specimens (including their 10–90 % scatter band. The corresponding effective crack sizes were derived from a statistical analysis of the defect population detected in the plain specimens through CT-based geometrical reconstruction. In line with Beretta's approach for identifying the most critical defect, the defect population was evaluated using

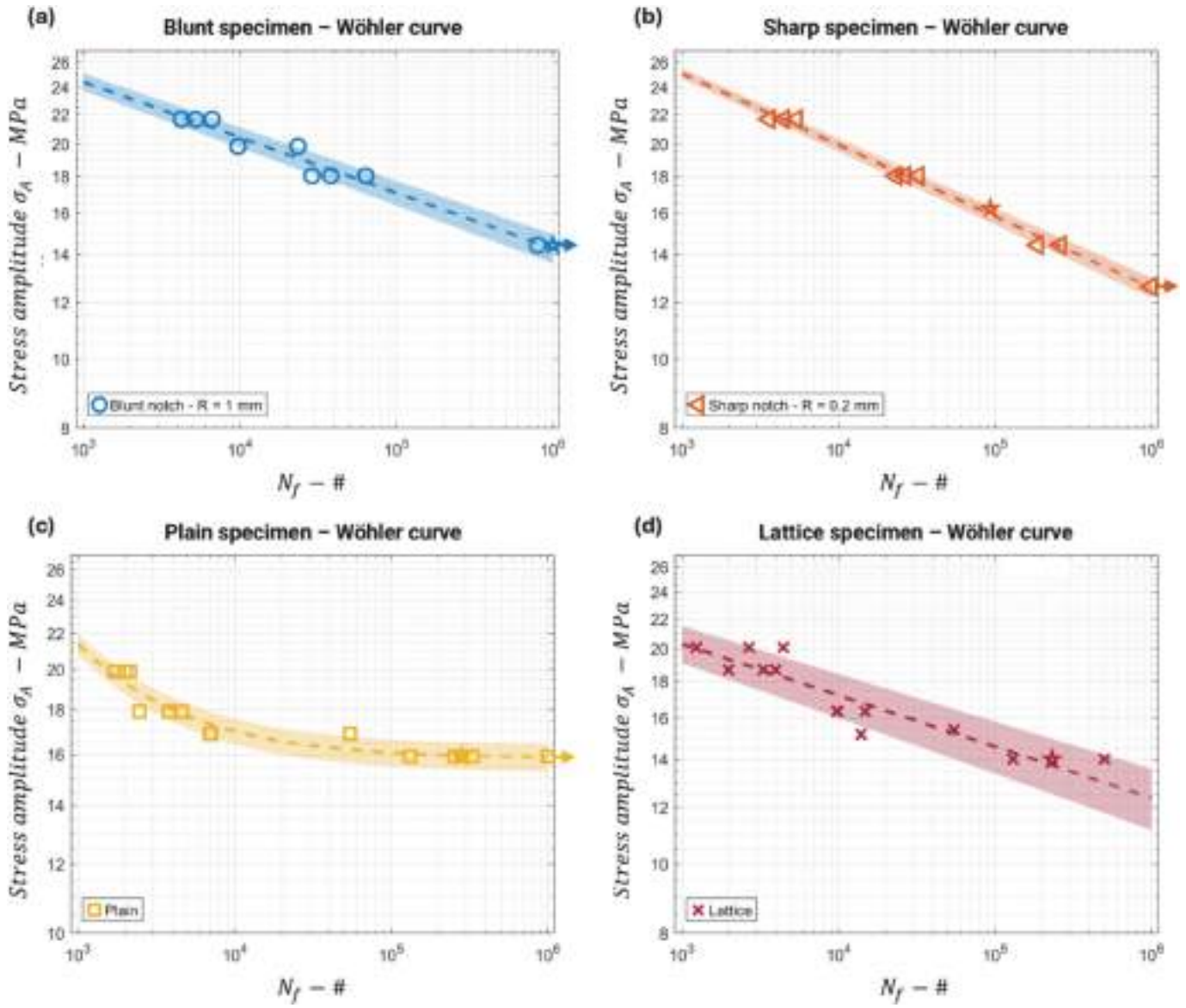

Fig. 11. Wöhler curves for blunt (a), sharp (b), plain (c), and lattice (d) specimens. Experimental data are fitted in accordance with Equation 1, and the scatter bands represent the 10%-90% failure probability. The specimens marked with a star were examined through fracture surface analysis, as shown in Fig. 10, while those indicated by an arrow correspond to run-outs.

Table 5
Fitting parameters for the fatigue curves and the standard deviation associated with the data distribution.

Geometry	C_1	C_2	C_3	Standard Deviation – MPa
Blunt notch	41.7621	0.077	–	0.52
Sharp notch	50.0388	0.099	–	0.32
Plain	583.94	0.674	15.82	0.44
Lattice	33.31	0.072	–	0.90

extreme-value statistics, enabling the estimation of the largest defect likely to control fatigue failure [75]. The peak over threshold (POT) approach is applied to the entire defect distribution – expressed as $\sqrt{\text{area}}$ – and the threshold is fixed to 0.25 mm after the observation of the mean excess plot depicted in Fig. 14a [76]. The resulting defect population is then fit with a generalized pareto distribution (GPD), as per Equation (11), and the defect dimension associated with the 99° percentile is computed and included in the KT diagram as characteristic dimension of the most critical defect statistically present in the plain specimen.

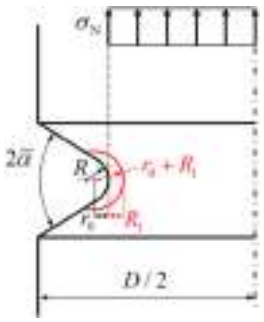

Fig. 12. Schematic representation of a notched specimen with all the characteristics dimensions needed for the ASED method characterization. In this scheme, D represents the specimen diameter, R_1 is the control radius and the dashed area represents the region Ω. The figure is []
adapted from 60.

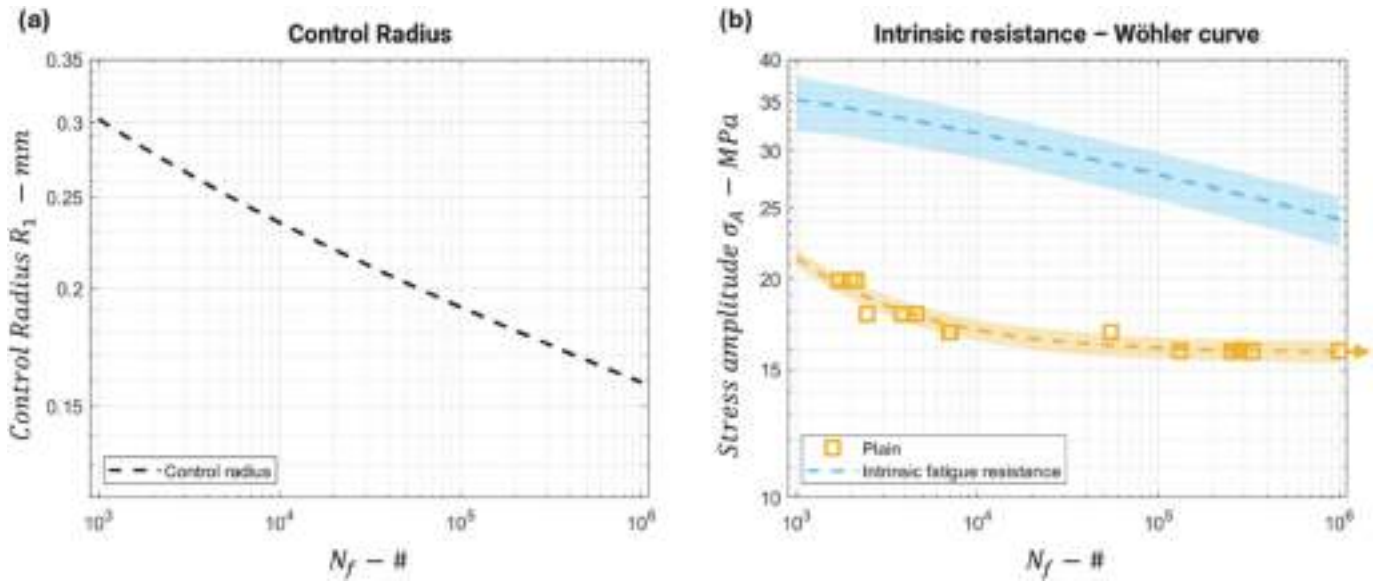

Fig. 13. a) control radius of the ased method vs. the number of cycles to failure. b) wöhler curves for plain specimens compared with the intrinsic fatigue resistance.

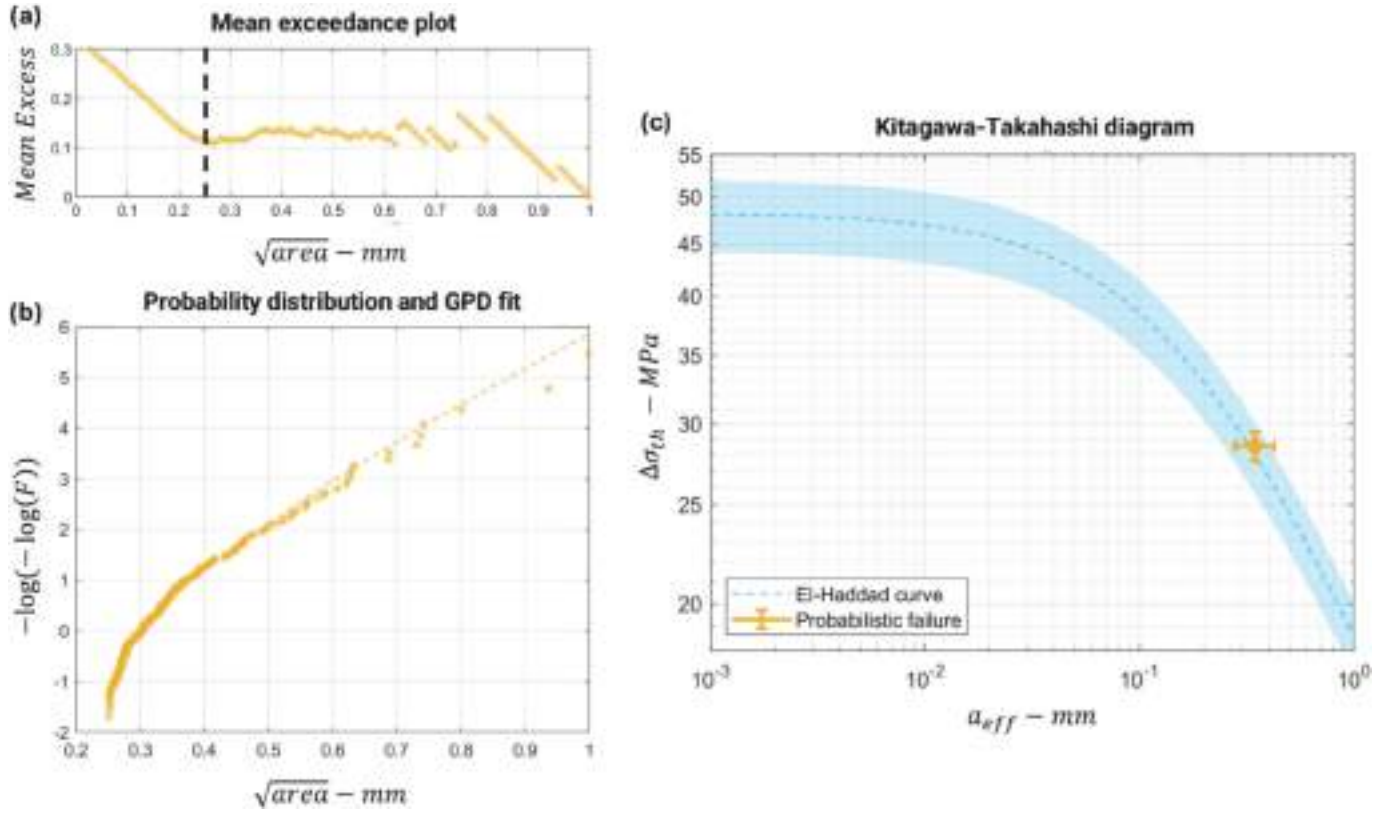

Fig. 14. (a) Mean excess plot for the identification of the threshold in the plain specimen defect distribution. The dotted vertical line represents graphically the selected threshold. (b) Probability distribution of the defect population and associated GPD fit computed with the maximum likelihood method. (c) Kitagawa–Takahashi diagram for plain specimens.

$$GPD(x) = 1 - \left(1 + \gamma\left(\frac{x-\lambda}{\delta}\right)\right)^{-\frac{1}{\gamma}} \tag{11}$$

The defect measure is corrected by the defect shape factor, considering these defects as surface-breaking defects $Y = 0.65$. Confidence intervals for the defect dimension are computed in agreement with [76]. The results of this statistical analysis are listed in Table 6.

To conclude, Fig. 14c shows that the plain specimens lie very close to the limit curve described by Eq. (10) in the KT diagram. This confirms the ability of the double-notch inversion method to identify intrinsic fatigue properties that accurately capture the influence of both manufacturing defects (in plain specimens) and geometrical stress concentrators (as in lattice structures), as further demonstrated in the next section.

Table 6
Results of the statistical analysis on the defect distribution expressed as $\sqrt{area}$ of the plain specimen.

γ	δ	λ
0.0568	0.1080	0.2500
99° percentile $-\sqrt{area}$		**a_{eff}- 99° percentile**
0.8182		0.3457

3.4. Fatigue prediction of lattice specimens

Taking advantage of the finite element model described in Section 2.5, several simulations were performed on the as-built geometry of the lattice structure to identify critical locations and associated critical ASED quantities, results are depicted in Fig. 15. The FE simulations were implemented by applying a vertical displacement on the upper surface of Fig. 4b corresponding to an axial force of 1 KN. After, different values of the ASED were calculated considering different values of the control radius. This task was accomplished by varying the radii of the spheres centered in points A and B and shown in Fig. 4d. In particular, the radii of the two bigger spheres were considered fixed and equal to 0.5 mm, while the radii of the two smaller spheres were varied and set equal to 0.3, 0.27, 0.24, 0.21, 0.18 and 0.15 mm. These latter values were also considered as the control radii for the ASED calculation. Once all the results were collected, the relationship between the ASED and the control radius was fitted, as shown in Fig. 16a, through a linear relationship, and the obtained correlation factor was equal to $R^2 = 0.978$. To calculate the ASED values for the experimental data, the fitted relationship was, firstly, evaluated in correspondence of the experimental control radii, then the obtained values were scaled considering the squared ratio between the experimental forces and the applied force during FE simulations, i.e. 1KN.

The ASED quantities computed thanks to the finite element simulations can be superimposed – in Fig. 15b – to the reference curve provided by the intrinsic fatigue resistance obtained in Fig. 13b. In agreement with [58], the fatigue resistance is charted in terms of $\Delta\overline{W}$ vs. number of cycles to failure and the associated scatter bands represent an error of ± 22% on the stresses.

A very good agreement is observed between the ASED values obtained from the finite element simulations of the lattice specimens and the reference curve derived from the intrinsic fatigue resistance of the bulk material. The lattice experimental points tend to fall on the upper side of the intrinsic curve, a behavior that may be attributed to differences in manufacturing history between lattice and bulk specimens, as well as to the greater ability of the lattice architecture to dissipate heat during cyclic loading compared with the bulkier notched geometries. Clearly, these hypotheses require confirmation through investigations that are currently underway.

Overall, this consistency confirms the capability of the proposed model to correctly identify the geometrically driven fatigue-critical locations in lattice structures, where manufacturing-induced defects do not dominate the failure mechanism. Consequently, when manufacturing quality is adequate, fatigue life estimation can reliably be performed directly on the as-designed lattice geometry in combination with the ASED criterion.

4. Conclusions

In this study, the fatigue behavior of Polyamide 12 (PA12) components manufactured by Multi Jet Fusion (MJF) was investigated through a combined experimental–numerical approach, with particular emphasis on extending the Average Strain Energy Density (ASED) method to complex lattice structures. The work integrated fatigue testing on bulk and notched specimens, CT-based defect characterization, fracture mechanics analyses, and finite element simulations on both bulk and lattice configurations.

Fatigue tests on plain specimens revealed a strong sensitivity to manufacturing-induced defects. CT-based reconstructions showed that large, isolated pores—absent at notch roots—critically reduced the fatigue strength of smooth samples, making them unsuitable for deriving intrinsic material properties. Conversely, sharp and blunt notched specimens, whose highly stressed volumes are far less affected by these large defects, provided reliable data for identifying the intrinsic fatigue strength and the ASED control radius through a double-notch inversion strategy.

Using the intrinsic ASED parameters, fatigue predictions for lattice specimens were successfully obtained from linear elastic FE simulations of the as-designed geometry, without requiring CT-based reconstruction. The close agreement between predictions and experiments confirms that fatigue performance in MJF-manufactured PA12 lattice structures is governed primarily by geometric stress concentrations rather than by the defect's population.

A further important outcome of this study is the demonstration that the intrinsic fatigue parameters derived from notched specimens also enable the construction of a Kitagawa–Takahashi (KT) diagram, which effectively quantifies the influence of manufacturing defects on plain specimens. The KT framework, supported by defect statistics from CT scans and long-crack threshold estimates derived from ASED parameters, proved capable of rationalizing the reduced fatigue strength observed in the plain geometry. This confirms the internal consistency of the proposed methodology and its ability to integrate defect-driven and geometry-driven fatigue mechanisms.

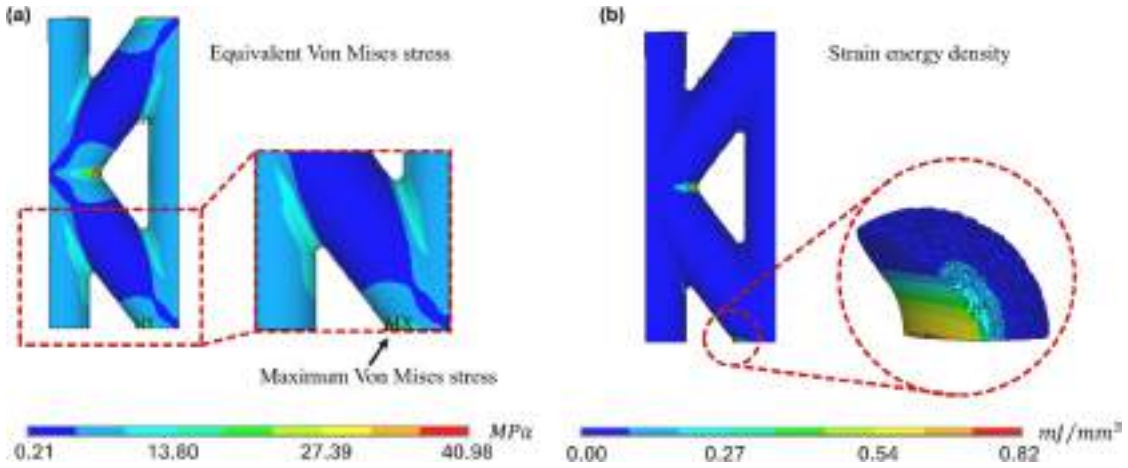

Fig. 15. Lattice specimen's finite element simulations results: a) von Mises stress distribution and b) strain energy density distribution.

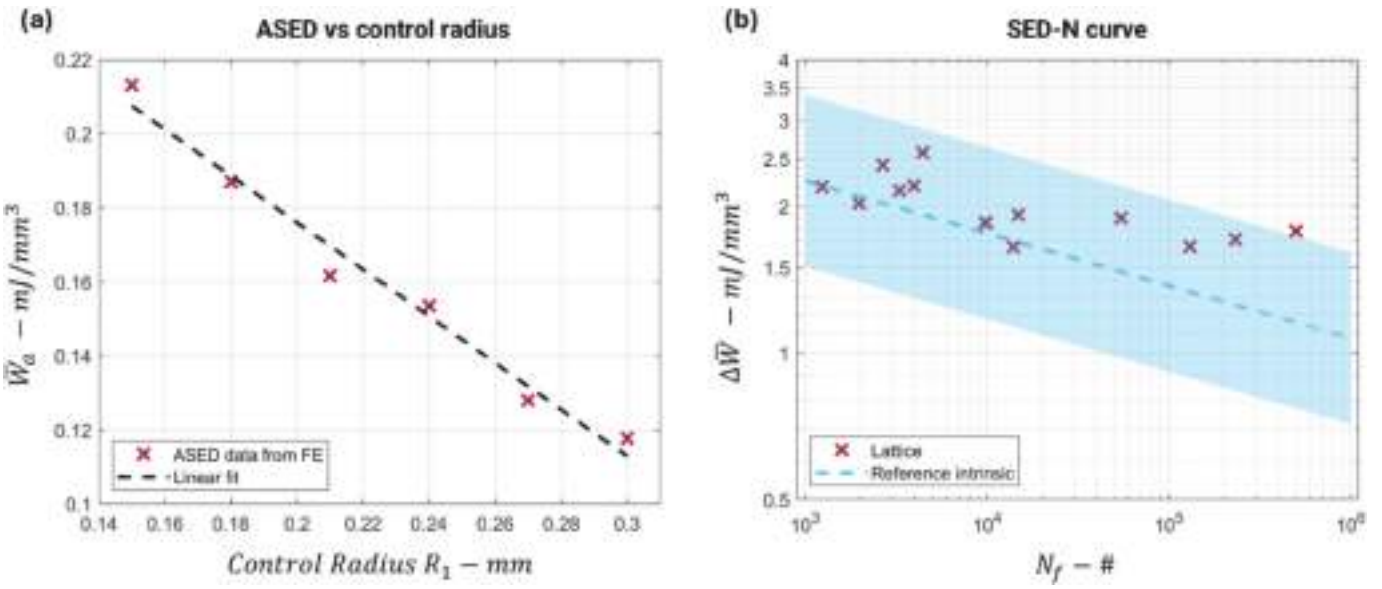

Fig. 16. Reference curve for PA12 MJF with the ASED results computed in agreement with the proposed methodology.

Overall, this work provides a validated and efficient methodology for fatigue life estimation of MJF PA12 lattice structures, supporting their broader adoption in lightweight and performance-critical applications where reliability and design freedom are essential.

Funding sources

Funded by the European Union (ERC, 101,093,897 Butterfly). Views and opinions expressed are however those of the author(s) only and do not necessarily reflect those of the European Union or the European Research Council Executive Agency. Neither the European Union nor the granting authority can be held responsible for them.

Declaration of Generative AI and AI-assisted technologies in the writing process

During the preparation of this work the authors used ChatGPT (based on GPT- 4o – OpenAI) to reorganize notes and improve the manuscript readability. After using this tool, the authors reviewed and edited the content as needed and took full responsibility for the content of the published article.

CRediT authorship contribution statement

Raffaele De Biasi: Writing – original draft, Visualization, Software, Methodology, Investigation, Formal analysis, Data curation, Conceptualization. **Lorenzo Romanelli:** Writing – original draft, Visualization, Software, Methodology. **Ciro Santus:** Writing – original draft, Visualization, Supervision, Software, Methodology, Conceptualization. **Matteo Perini:** Writing – review & editing, Resources. **Filippo Berto:** Writing – review & editing, Supervision, Funding acquisition. **Matteo Benedetti:** Writing – original draft, Supervision, Software, Methodology, Formal analysis, Data curation, Conceptualization.

Declaration of competing interest

The authors declare that they have no known competing financial interests or personal relationships that could have appeared to influence the work reported in this paper.

Acknowledgments

The authors would like to thank Gianluca Berti, Ciro Malacarne from ProM Facility and Damiano. Foltran for their support in the success of this work.

Appendix A. Supplementary material

Supplementary data to this article can be found online at https://doi.org/10.1016/j.ijfatigue.2025.109452.

Data availability

Data will be made available on request.

References

[1] Emanuelli L, Jam A, du Plessis A, Lora C, De Biasi R, Benedetti M, et al. Manufacturability of functionally graded porous β-Ti21S auxetic architected biomaterials produced by laser powder bed fusion: Comparison between 2D and 3D metrological characterization. Int J Bioprint 2023;9(728).

[2] Ráž K, Chval Z, Pereira M. Lattice structures—mechanical description with respect to additive manufacturing. Materials 2024;17:5298. https://doi.org/10.3390/ma17215298.

[3] De Biasi R, Murchio S, Sbettega E, Carmignato S, Luchin V, Benedetti M. Efficient optimization framework for L-PBF fatigue enhanced Ti6Al4V lattice component. Mater Des 2023;230:111975. https://doi.org/10.1016/j.matdes.2023.111975.

[4] De Biasi R, Yasin MS, Perini M, Benedetti M, Berto F. Compensated beam model for efficient and accurate FE elastic simulation of strut-based lattice structures. Mater Des 2025;255:114213. https://doi.org/10.1016/j.matdes.2025.114213.

[5] Ráž K, Chval Z, Kemka V. Parametric production of prostheses using the additive polymer manufacturing technology multi jet fusion. Materials 2024;17:2347. https://doi.org/10.3390/ma17102347.

[6] Romanelli L, Santus C, Senegaglia I, Tamburrino F, Controzzi M, Corrado A, et al. Lightweight design of polymeric thin-walled components: latticization and elastic–plastic homogenization. J Mater Res Technol 2025;36:2977–93. https://doi.org/10.1016/j.jmrt.2025.03.137.

[7] Gao P, Liu R, Wang M, Zhang H, Gao X, Ma J. Static and fatigue behaviors of polyamide 12 hinge joint manufactured by multi-jet fusion. J Mater Eng Perform 2025;34:6879–90. https://doi.org/10.1007/s11665-024-09661-7.

[8] Morales-Planas S, Minguella-Canela J, Lluma-Fuentes J, Travieso-Rodriguez JA, García-Granada A-A. Multi jet fusion PA12 manufacturing parameters for watertightness. Strength Tolerances Materials 2018;11:1472. https://doi.org/10.3390/ma11081472.

[9] Zhu Z, Majewski C. Understanding pore formation and the effect on mechanical properties of High speed Sintered polyamide-12 parts: a focus on energy input. Mater Des 2020;194:108937. https://doi.org/10.1016/j.matdes.2020.108937.

[10] Kusoglu IM, Doñate-Buendía C, Barcikowski S, Gökce B. Laser powder bed fusion of polymers: quantitative research direction indices. Materials 2021;14:1169. https://doi.org/10.3390/ma14051169.

[11] Sillani F, MacDonald E, Villela J, Schmid M, Wegener K. In-situ monitoring of powder bed fusion of polymers using laser profilometry. Addit Manuf 2022;59:103074. https://doi.org/10.1016/j.addma.2022.103074.

[12] Van Hooreweder B, Moens D, Boonen R, Kruth J-P, Sas P. On the difference in material structure and fatigue properties of nylon specimens produced by injection

molding and selective laser sintering. Polym Test 2013;32:972–81. https://doi.org/10.1016/j.polymertesting.2013.04.014.
[13] Dupin S, Lame O, Barrès C, Charmeau J-Y. Microstructural origin of physical and mechanical properties of polyamide 12 processed by laser sintering. Eur Polym J 2012;48:1611–21. https://doi.org/10.1016/j.eurpolymj.2012.06.007.
[14] Jabri FE, Ouballouch A, Lasri L, El Alaiji R. A comprehensive review of polymer materials and selective laser sintering technology for 3D printing. J Achiev Mater Manufact Eng 2023;118:5–17. https://doi.org/10.5604/01.3001.0053.7286.
[15] Kim H, Zhao Y, Zhao L. Process-level modeling and simulation for HP's Multi Jet Fusion 3D printing technology. 2016 1st International Workshop on Cyber-Physical Production Systems (CPPS), IEEE; 2016. 10.1109/cpps.2016.7483916.
[16] O'Connor HJ, Dickson AN, Dowling DP. Evaluation of the mechanical performance of polymer parts fabricated using a production scale multi jet fusion printing process. Addit Manuf 2018;22:381–7. https://doi.org/10.1016/j.addma.2018.05.035.
[17] Riedelbauch J, Rietzel D, Witt G. Analysis of material aging and the influence on the mechanical properties of polyamide 12 in the Multi Jet Fusion process. Addit Manuf 2019;27:259–66. https://doi.org/10.1016/j.addma.2019.03.002.
[18] Galati M, Calignano F, Defanti S, Denti L. Disclosing the build-up mechanisms of multi jet fusion: Experimental insight into the characteristics of starting materials and finished parts. J Manuf Process 2020;57:244–53. https://doi.org/10.1016/j.jmapro.2020.06.029.
[19] da Silva R, Wessling Oening Dicati G, Gubaua JE, Radovanovic E, Favaro SL. Evaluation of the mechanical properties of polyamide 12 regarding different percentages of reused material in the selective laser sintering process. Rapid Prototyp J 2023;29:2134–48. https://doi.org/10.1108/rpj-03-2023-0091.
[20] Cai C, Tey WS, Chen J, Zhu W, Liu X, Liu T, et al. Comparative study on 3D printing of polyamide 12 by selective laser sintering and multi jet fusion. J Mater Process Technol 2021;288:116882. https://doi.org/10.1016/j.jmatprotec.2020.116882.
[21] Shu J, Wang J, Li Z, Tong R-K-Y. Effects of slit edge notches on mechanical properties of 3D-printed PA12 nylon kirigami specimens. Polymers (Basel) 2023;15:3082. https://doi.org/10.3390/polym15143082.
[22] Lammens N, Kersemans M, De Baere I, Van Paepegem W. On the visco-elasto-plastic response of additively manufactured polyamide-12 (PA-12) through selective laser sintering. Polym Test 2017;57:149–55. https://doi.org/10.1016/j.polymertesting.2016.11.032.
[23] Sillani F, Kleijnen RG, Vetterli M, Schmid M, Wegener K. Selective laser sintering and multi jet fusion: Process-induced modification of the raw materials and analyses of parts performance. Addit Manuf 2019;27:32–41. https://doi.org/10.1016/j.addma.2019.02.004.
[24] Xu Z, Wang Y, Wu D, Ananth KP, Bai J. The process and performance comparison of polyamide 12 manufactured by multi jet fusion and selective laser sintering. J Manuf Process 2019;47:419–26. https://doi.org/10.1016/j.jmapro.2019.07.014.
[25] Sagradov I, Schob D, Roszak R, Maasch P, Sparr H, Ziegenhorn M. Experimental investigation and numerical modelling of 3D printed polyamide 12 with viscoplasticity and a crack model at different strain rates. Mater Today Commun 2020;25:101542. https://doi.org/10.1016/j.mtcomm.2020.101542.
[26] Rosso S, Meneghello R, Biasetto L, Grigolato L, Concheri G, Savio G. In-depth comparison of polyamide 12 parts manufactured by Multi Jet Fusion and Selective Laser Sintering. Addit Manuf 2020;36:101713. https://doi.org/10.1016/j.addma.2020.101713.
[27] Schneider J, Kumar S. Multiscale characterization and constitutive parameters identification of polyamide (PA12) processed via selective laser sintering. Polym Test 2020;86:106357. https://doi.org/10.1016/j.polymertesting.2020.106357.
[28] Santonocito D. Evaluation of fatigue properties of 3D-printed Polyamide-12 by means of energy approach during tensile tests. Procedia Struct Integrity 2020;25:355–63. https://doi.org/10.1016/j.prostr.2020.04.040.
[29] Hofland EC, Baran I, Wismeijer DA. Correlation of process parameters with mechanical properties of laser sintered PA12 parts. Adv Mater Sci Eng 2017;2017:1–11. https://doi.org/10.1155/2017/4953173.
[30] Le KQ, Tran VT, Chen K, Teo HWB, Zeng J, Zhou K, et al. Predicting crystallinity of polyamide 12 in multi jet fusion process. J Manuf Process 2023;99:1–11. https://doi.org/10.1016/j.jmapro.2023.05.043.
[31] Perez-Barcenilla S, Cearsolo X, Aramburu A, Castano-Alvarez R, Castillo JR, Gayoso LJ. Applicability of a material constitutive model based on a transversely isotropic behaviour for the prediction of the mechanical performance of multi jet fusion printed polyamide 12 parts. Polymers (Basel) 2024;16:56. https://doi.org/10.3390/polym16010056.
[32] Barriere T, Carbillet S, Gabrion X, Holopainen S. Prediction of short- to long-term cyclic deformation behavior and fatigue life of polymers. Polymers (Basel) 2024;16:1640. https://doi.org/10.3390/polym16121640.
[33] Sadananda K, Vasudevan AK. Analysis of fatigue crack growth behavior in polymers using the unified approach. Mater Sci Eng A 2004;387–389:536–41. https://doi.org/10.1016/j.msea.2004.01.115.
[34] Cano AJ, Salazar A, Rodríguez J. Evaluation of different crack driving forces for describing the fatigue crack growth behaviour of PET-G. Int J Fatigue 2018;107:27–32. https://doi.org/10.1016/j.ijfatigue.2017.10.013.
[35] Ezeh OH, Susmel L. Fatigue strength of additively manufactured polylactide (PLA): effect of raster angle and non-zero mean stresses. Int J Fatigue 2019;126:319–26. https://doi.org/10.1016/j.ijfatigue.2019.05.014.
[36] Boukhili R, Decharentenay F, Vukhanh T. Effect of frequency and orientation on fatigue crack propagation in polyamide-12. Int J Fatigue 1986;8:127–34. https://doi.org/10.1016/0142-1123(86)90003-4.
[37] Salazar A, Cano AJ, Rodríguez J. Fatigue life assessment of polyamide 12 processed by selective laser sintering. Damage modelling according to fracture mechanics. Rapid Prototyp J 2022;28:814–23. https://doi.org/10.1108/rpj-06-2021-0142.
[38] Cano AJ, Salazar A, Rodríguez J. Effect of the orientation on the fatigue crack growth of polyamide 12 manufactured by selective laser sintering. Rapid Prototyp J 2019;25:820–9. https://doi.org/10.1108/rpj-09-2018-0255.
[39] Chen K, Teo HWB, Tian Y, Wu S, Kang G, Zhou K, et al. Effect of build direction on tension–tension low cycle fatigue behavior of polyamide 12 parts printed by Multi Jet fusion. Int J Fatigue 2023;170:107514. https://doi.org/10.1016/j.ijfatigue.2023.107514.
[40] Kitagawa H, Takahashi S. Applicability of fracture mechanics to very small cracks or the cracks in the early stage. In: for Metals MPAS, editor. Proceedings of second international conference on mechanical behaviour of materials, Cleveland, Ohio: 1976, p. 627–31.
[41] El Haddad MH, Topper TH, Smith KN. Prediction of non propagating cracks. Eng Fract Mech 1979;11:573–84. https://doi.org/10.1016/0013-7944(79)90081-x.
[42] Beretta S, Romano S. A comparison of fatigue strength sensitivity to defects for materials manufactured by AM or traditional processes. Int J Fatigue 2017;94:178–91. https://doi.org/10.1016/j.ijfatigue.2016.06.020.
[43] Benedetti M, Santus C. Building the Kitagawa-Takahashi diagram of flawed materials and components using an optimized V-notched cylindrical specimen. Eng Fract Mech 2020;224:106810. https://doi.org/10.1016/j.engfracmech.2019.106810.
[44] Salazar A, Cano AJ, Rodríguez J. Mechanical and fatigue behaviour of polyamide 12 processed via injection moulding and selective laser sintering. Analysis based on Kitagawa-Takahashi diagrams. Eng Fract Mech 2022;275:108825. https://doi.org/10.1016/j.engfracmech.2022.108825.
[45] Schob D, Sagradov I, Roszak R, Sparr H, Franke R, Ziegenhorn M, et al. Experimental determination and numerical simulation of material and damage behaviour of 3D printed polyamide 12 under cyclic loading. Eng Fract Mech 2020;229:106841. https://doi.org/10.1016/j.engfracmech.2019.106841.
[46] Van Hooreweder B, Kruth J-P. High cycle fatigue properties of selective laser sintered parts in polyamide 12. CIRP Ann 2014;63:241–4. https://doi.org/10.1016/j.cirp.2014.03.060.
[47] Van Hooreweder B, De Coninck F, Moens D, Boonen R, Sas P. Microstructural characterization of SLS-PA12 specimens under dynamic tension/compression excitation. Polym Test 2010;29:319–26. https://doi.org/10.1016/j.polymertesting.2009.12.006.
[48] D'Andrea D, Crisafulli D, Risitano G, Santonocito D. Rapid fatigue life evaluation over time of PA12 obtained by Multijet Fusion printing process. Int J Fatigue 2025;200:109124. https://doi.org/10.1016/j.ijfatigue.2025.109124.
[49] Ahmed AA, Susmel L. A material length scale–based methodology to assess static strength of notched additively manufactured polylactide (PLA). Fatigue Fract Eng Mater Struct 2018;41:2071–98. https://doi.org/10.1111/ffe.12746.
[50] Ezeh OH, Susmel L. On the notch fatigue strength of additively manufactured polylactide (PLA). Int J Fatigue 2020;136:105583. https://doi.org/10.1016/j.ijfatigue.2020.105583.
[51] Crespo M, Gómez-del Río T, Rodríguez J. Failure of polyamide 12 notched samples manufactured by selective laser sintering. J Strain Anal Eng Des 2019;54:192–8. https://doi.org/10.1177/0309324719847817.
[52] Avanzini A, Battini D, Pandini S. Static and fatigue behavior in presence of notches for polyamide 12 (PA12) additively manufactured via Multi Jet Fusion™ process. Int J Fatigue 2022;161:106912. https://doi.org/10.1016/j.ijfatigue.2022.106912.
[53] Susmel L, Taylor D. The Theory of critical Distances as an alternative experimental strategy for the determination of KIc and ΔKth. Eng Fract Mech 2010;77:1492–501. https://doi.org/10.1016/j.engfracmech.2010.04.016.
[54] Santus C, Taylor D, Benedetti M. Determination of the fatigue critical distance according to the Line and the Point Methods with rounded V-notched specimen. Int J Fatigue 2018;106:208–18. https://doi.org/10.1016/j.ijfatigue.2017.10.002.
[55] Santus C, Taylor D, Benedetti M. Experimental determination and sensitivity analysis of the fatigue critical distance obtained with rounded V-notched specimens. Int J Fatigue 2018;113:113–25. https://doi.org/10.1016/j.ijfatigue.2018.03.037.
[56] Santus C, Berto F, Pedranz M, Benedetti M. Mode III critical distance determination with optimized V-notched specimen under torsional fatigue and size effects on the inverse search probability distribution. Int J Fatigue 2021;151:106351. https://doi.org/10.1016/j.ijfatigue.2021.106351.
[57] Romanelli L, Santus C, Macoretta G, Barsanti M, Monelli BD, Senegaglia I, et al. A TCD-based statistical method to assess the impact of surface roughness and pores on the fatigue strength of LPBF Inconel 718 specimens. Int J Fatigue 2025;194:108821. https://doi.org/10.1016/j.ijfatigue.2025.108821.
[58] De Biasi R, Oztoprak O, Zanini F, Carmignato S, Kollmannsberger S, Benedetti M. Predicting fatigue life of additively manufactured lattice structures using the image-based Finite Cell Method and average strain energy density. Mater Des 2024;246:113321. https://doi.org/10.1016/j.matdes.2024.113321.
[59] Benedetti M, Santus C, Berto F. Inverse determination of the fatigue Strain Energy Density control radius for conventionally and additively manufactured rounded V-notches. Int J Fatigue 2019;126:306–18. https://doi.org/10.1016/j.ijfatigue.2019.04.040.
[60] Benedetti M, Dallago M, Santus C. Statistical significance of notch fatigue prognoses based on the strain-energy–density method: Application to conventionally and additively manufactured materials. Theor Appl Fract Mech 2020;109:102720. https://doi.org/10.1016/j.tafmec.2020.102720.
[61] Benedetti M, Pedranz M, Berto F, Santus C. Inverse determination and probability distribution of the mode III strain energy density control radius with an optimized V-notched specimen under torsional fatigue loading. Int J Fatigue 2022;159:106787. https://doi.org/10.1016/j.ijfatigue.2022.106787.
[62] Pedranz M, Fontanari V, Raghavendra S, Santus C, Zanini F, Carmignato S, et al. A new energy based highly stressed volume concept to investigate the notch-pores

interaction in thick-walled ductile cast iron subjected to uniaxial fatigue. Int J Fatigue 2023;169:107491. https://doi.org/10.1016/j.ijfatigue.2022.107491.
[63] Pedranz M, Fontanari V, Santus C, Lusuardi D, Berto F, Benedetti M. A strain energy density design approach for large cast iron components: from microstructural analysis to multiaxial fatigue response. Int J Fatigue 2023;175:107824. https://doi.org/10.1016/j.ijfatigue.2023.107824.
[64] Pedranz M, Fontanari V, De Biasi R, Berto F, Santus C, Benedetti M. A simplified strain energy density approach for multiaxial fatigue predictions. Int J Mech Sci 2025;288:109961. https://doi.org/10.1016/j.ijmecsci.2025.109961.
[65] Avanzini A, Tomasoni M, Xu Z, Berto F, Razavi N. Fracture assessment of polyamide 12 (PA12) specimens fabricated via Multi Jet FusionTM in the presence of geometrical discontinuities. Eng Fract Mech 2024;303:110118. https://doi.org/10.1016/j.engfracmech.2024.110118.
[66] Zolfagharian A, Khosravani MR, Kaynak A. Fracture resistance analysis of 3D-printed polymers. Polymers (Basel) 2020;12:302. https://doi.org/10.3390/polym12020302.
[67] Calignano F, Giuffrida F, Galati M. Effect of the build orientation on the mechanical performance of polymeric parts produced by multi jet fusion and selective laser sintering. J Manuf Process 2021;65:271–82. https://doi.org/10.1016/j.jmapro.2021.03.018.
[68] Abbott CS, Sperry M, Crane NB. Relationships between porosity and mechanical properties of polyamide 12 parts produced using the laser sintering and multi-jet fusion powder bed fusion processes. J Manuf Process 2021;70:55–66. https://doi.org/10.1016/j.jmapro.2021.08.012.
[69] Adach M, Sokołowski P, Piwowarczyk T, Nowak K. Study on Geometry, Dimensional Accuracy and Structure of Parts Produced by Multi Jet Fusion. Materials 2021;14:4510. https://doi.org/10.3390/ma14164510.
[70] Murakami Y, Endo M. Effects of defects, inclusions and inhomogeneities on fatigue strength. Int J Fatigue 1994;16:163–82. https://doi.org/10.1016/0142-1123(94)90001-9.
[71] Sauer JA, Richardson GC. Fatigue of polymers. Int J Fract 1980;16:499–532. https://doi.org/10.1007/BF02265215.
[72] Kitagawa H, Takahashi S. Applicability of fracture mechanics to very small cracks or the cracks in the early stage. Proc Second Int Conf Mech Behav Mater 1976:627–31.
[73] Lazzarin P, Berto F. From Neuber's elementary volume to kitagawa and atzori's diagrams: an interpretation based on local energy. Int J Fract 2005;135:L33–8. https://doi.org/10.1007/s10704-005-4393-x.
[74] Meneghetti G, Rigon D, Gennari C. An analysis of defects influence on axial fatigue strength of maraging steel specimens produced by additive manufacturing. Int J Fatigue 2019;118:54–64. https://doi.org/10.1016/j.ijfatigue.2018.08.034.
[75] Beretta S. More than 25 years of extreme value statistics for defects: Fundamentals, historical developments, recent applications. Int J Fatigue 2021;151:106407. https://doi.org/10.1016/j.ijfatigue.2021.106407.
[76] Romano S, Brandão A, Gumpinger J, Gschweitl M, Beretta S. Qualification of AM parts: Extreme value statistics applied to tomographic measurements. Mater Des 2017;131:32–48. https://doi.org/10.1016/j.matdes.2017.05.091.